Available online at www.sciencedirect.com

ScienceDirect

ELSEVIER

Coordination Chemistry Reviews 250 (2006) 2271–2294

COORDINATION CHEMISTRY REVIEWS

www.elsevier.com/locate/ccr

Review

Electronic structures of highly deformed iron(III) porphyrin complexes

Mikio Nakamura [a,b,c,*]

[a] *Department of Chemistry, School of Medicine, Toho University, Ota-ku, Tokyo 143-8540, Japan*
[b] *Division of Chemistry, Graduate School of Science, Toho University, Funabashi 274-8510, Japan*
[c] *Research Center for Materials with Integrated Properties, Toho University, Funabashi 274-8510, Japan*

Received 12 September 2005; accepted 2 March 2006
Available online 17 April 2006

Contents

1. Introduction 2272
2. Electron configurations of low-spin complexes 2272
   2.1. General consideration 2272
   2.2. Spectroscopic studies on the effect of porphyrin deformation 2275
      2.2.1. ^{1}H NMR spectroscopy 2275
      2.2.2. ^{13}C NMR spectra 2276
      2.2.3. EPR spectra 2278
   2.3. Electron configurational isomers 2279
3. Mixed high-spin and intermediate-spin state 2280
   3.1. General Consideration 2280
   3.2. Effect of ruffled porphyrin ring on the spin state 2282
      3.2.1. Five-coordinate complexes 2282
      3.2.2. Six-coordinate complexes 2283
   3.3. Effect of saddled porphyrin ring on the spin state 2284
      3.3.1. Five-coordinate complexes 2284
      3.3.2. Six-coordinate complexes 2284
4. Spin-crossover in saddled complexes 2285
   4.1. General consideration 2285
   4.2. Magnetic behavior in solution 2285
      4.2.1. $[Fe(OETPP)L_2]^+$ 2285
      4.2.2. $Fe(OMTPP)L_2^+$ 2287
   4.3. Magnetic behavior in the solid 2287
      4.3.1. $Fe(OETPP)L_2^+$ 2287
      4.3.2. $Fe(OMTPP)L_2^+$ 2288
      4.3.3. Structural consequences of spin crossover 2289
      4.3.4. Importance of crystal packing 2290
5. Conclusions 2292
   Acknowledgments 2292
   References 2292

Abbreviations: TPP, 5,10,15,20-tetraphenylporphyrin; TMP, 5,10,15,20-tetramesitylpoprhyrin; THP, porphin; TEtP, 5,10,15,20-tetraethylporphyrin; T^{n}PrP, 5,10,15,20-tetrapropylporphyrin; T^{c}PrP, 5,10,15,20-tetracyclopropylporphyrin; T^{i}PrP, 5,10,15,20-tetraisopropylporphyrin; TEtPrP, 5,10,15,20-tetrakis(1-ethylpropyl)porphyrin; TMCP, 5,10,15,20-tetramethylchiroporphyrin; TCHP, 5,10,15,20-tetracyclohexylporphyrin; TRP, 5,10,15,20-tetraalkylporphyrin; TArP, 5,10,15,20-tetraarylporphyrin; OMTPP, 2,3,7,8,12,13,17,18-octamethyl-5,10,15,20-tetraphenylporphyrin; OETPP, 2,3,7,8,12,13,17,18-octaethyl-5,10,15,20-tetraphenylporphyrin; TMTMP, 3,8,13,18-tetramesityl-2,7,12,17-tetramethylporphyrin; TPrPc, 2,7,12,17-tetrapropylporphycene; HIm, imidazole; 2-MeIm, 2-methylimidazole; 2-MeBzIm, 2-methylbenzimidazole; DMAP, 4-(*N*,*N*-dimethylamino)pyridine; Py, pyridine; 3-CNPy, 3-cyanopyridine; 4-CNPy, 4-cyanopyridine; ^{t}BuNC, *tert*-butylisocyanide

* Tel.: +81 337624151; fax: +81 354935430.
E-mail address: mnakamu@med.toho-u.ac.jp.

0010-8545/$ – see front matter © 2006 Elsevier B.V. All rights reserved.
doi:10.1016/j.ccr.2006.03.001

Abstract

This review describes the effects of highly deformed porphyrin ring on the electronic structures of iron(III) porphyrinates, which includes (i) the electron configurations in low-spin ($S = 1/2$) ruffled complexes, (ii) the contribution of the intermediate-spin ($S = 3/2$) state in the spin-admixed ($S = 5/2$, 3/2) complexes with ruffled and saddled porphyrin ring, and (iii) the novel spin crossover ($S = 1/2$, $S = 3/2$) phenomenon in saddled complexes, with a special emphasis on the use of ^{1}H NMR, ^{13}C NMR, and EPR spectroscopy.
© 2006 Elsevier B.V. All rights reserved.

Keywords: Porphyrin; Iron(III); Deformation; Electronic structures; NMR; EPR; Spin crossover

1. Introduction

Elucidation of the electronic structures of iron porphyrin complexes is quite important to understand the function and catalytic processes of naturally occurring heme proteins. A number of techniques have been used to solve this problem, which include UV–vis, NMR, EPR, resonance Raman, MCD, Mössbauer, EXAFS, SQUID, X-ray crystallography, etc. [1]. Among these techniques, ^{1}H NMR is particularly useful because it serves a detailed information on the electronic structures of the complexes in solution at various temperatures [2–9]. This is because the iron d orbital with an unpaired electron interacts with the specific π molecular orbitals of porphyrin and increases the π spin density at the specific carbon and nitrogen atoms of the complex. Consequently, the NMR signals of the protons directly attached to, or attached by two bonds, to the carbon atom exhibit upfield or downfield shifts, respectively. In addition, the unpaired electrons in the $d_{x^2-y^2}$ and d_{z^2} orbitals can be delocalized through σ bonds to the protons and induce downfield shifts of the proton signals. Thus, we can determine which d orbital has unpaired electron by the analysis of the observed ^{1}H NMR chemical shifts. In other words, the chemical shift can be a good probe to reveal the electronic structure of iron(III) porphyrin complexes. Through the extensive studies using ^{1}H NMR spectroscopy, it is now clear that the spin states of iron(III) porphyrin complexes are controlled by the nature and number of the axial ligands. While the six-coordinate complexes carrying axial ligands with strong field strength such as imidazole and cyanide exhibit a low-spin ($S = 1/2$) state, the five-coordinate complexes carrying an anionic ligand such as halide and acetate show a high-spin ($S = 5/2$) state. If the field strengths of anionic ligands become fairly weak, the complexes adopt a rare intermediate-spin ($S = 3/2$) state as shown in Fig. 1.

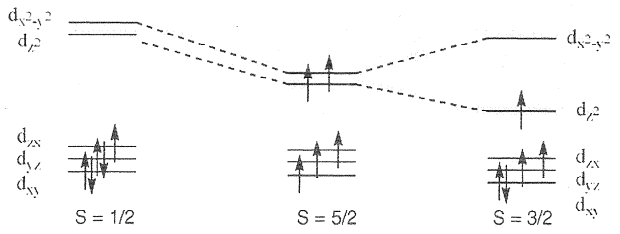

Fig. 1. Spin states of iron(III) porphyrin complexes.

In addition to the field strength of the axial ligands, deformation of the porphyrin ring [10,11] also affects the electronic structures of the iron(III) porphyrin complexes. This is because some specific interactions, which are forbidden in planar complexes, are allowed if the porphyrin ring is deformed [12–15]. Consequently, the energy levels of the five d orbitals are perturbed to give a unique electronic structure. Since the porphyrin deformation is commonly observed in naturally occurring heme proteins [16–20], it is very important to elucidate the effect of porphyrin deformation on the physicochemical properties of the complexes. Because many good review articles describing the electronic structures of hemes and model heme complexes have been published [2–9,21–23], this review article focuses on how the porphyrin deformation, especially the ruffling or saddling, affects the spin states and electron configurations of iron(III) porphyrin complexes with an emphasis on the use of ^{1}H NMR, ^{13}C NMR, and EPR spectroscopy. As shown in Fig. 2, the ruffling of the porphyrin core indicates that the *meso* carbon atoms deviate from the mean porphyrin plane up and down alternately [24–27], while the saddling of the porphyrin core indicates that the β carbon atoms deviate similarly [28–30].

2. Electron configurations of low-spin complexes

2.1. General consideration

There are two types of electronic ground state in low-spin iron(III) porphyrin complexes. One is the commonly observed ground state with the $(d_{xy})^2(d_{xz}, d_{yz})^3$ electron configuration

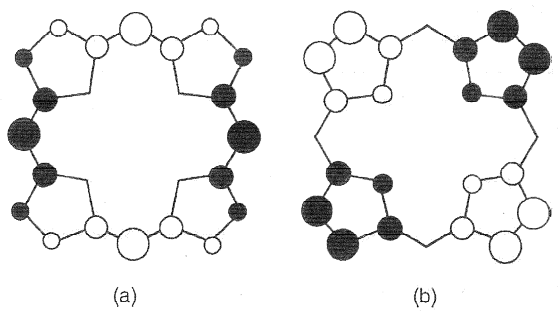

Fig. 2. Major deformation modes of porphyrin: (a) ruffle and (b) saddle. Open circles represent atoms above the least-squares plane, and the filled circles correspond to atoms below the plane.

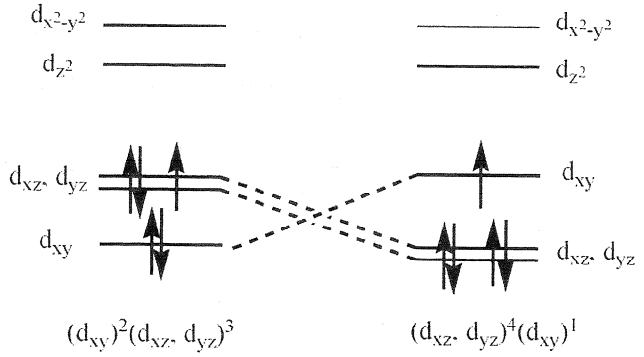

Fig. 3. Electron configurations of low spin iron(III) complexes.

and the other is the less common ground state with the $(d_{xz}, d_{yz})^4(d_{xy})^1$ electron configuration as shown in Fig. 3 [3]. Recent studies have revealed that the ground state of low-spin complexes is controlled by the electronic nature of axial ligands [3]. Although the complexes carrying axial ligands with strong σ-donating ability such as imidazole and cyanide adopt the common $(d_{xy})^2(d_{xz}, d_{yz})^3$ state, the complexes carrying axial ligands with weak σ-donating and strong π-accepting ability such as *tert*-BuNC and 4-CNPy prefer the less common $(d_{xz}, d_{yz})^4(d_{xy})^1$ state. Walker, Scheidt and others explained that the d_π orbitals of these complexes are stabilized by the interaction with the low-lying $p_{\pi*}$ orbital of the ligand to the point where they lie lower than the d_{xy} orbital [31–33]. As a result, the unpaired electron occupies the d_{xy} orbital to form the $(d_{xz}, d_{yz})^4(d_{xy})^1$ electron configuration. Depending on the energy difference between the d_{xy} and d_π orbitals, the excited state with the different electron configurations contributes to the electronic state of the complex. If the d_{xy} orbital is located far above the d_π orbitals in energy diagram, then the complex has a quite pure $(d_{xz}, d_{yz})^4(d_{xy})^1$ ground state. If, on the other hand, the energy difference is rather small, then the contribution of the excited state increases. The spectroscopic properties of the complex, therefore, change depending on the energy difference between the d_{xy} and d_π orbitals.

Electron configuration of the low-spin complexes causes tremendous influence on the ^{1}H NMR spectra. In the case of the $(d_{xy})^2(d_{xz}, d_{yz})^3$ type complexes, the unpaired electron in the iron d_π orbitals delocalizes to the porphyrin ring through the interaction with the porphyrin($3e_g$) orbitals. Because the $3e_g$ orbital has sizable coefficients on the β-pyrrole carbon and nitrogen atoms and zero coefficient on the *meso* carbon atoms as shown in Fig. 4, the interaction shifts the pyrrole-H signal to the upfield position [2–9]. Typical example is $[Fe(TPP)(CN)_2]^-$ where the pyrrole-II, *o*-, *m*-, and *p*-H signals appear at −16.55, 4.55, 6.36, and 6.08 ppm in CD_2Cl_2 at 298 K, respectively [34]. For many years, the presence of the upfield shifted pyrrole-H signal was considered to be the condition that all the TPP type low-spin complexes must satisfy. In 1989, Simonneaux et al. reported that low-spin $[Fe(TPP)(^tBuNC)_2]^+$ shows a completely different ^{1}H NMR spectrum [35,36]. The pyrrole-H, *o*-, *m*-, and *p*-H signals appear at 9.73, 0.96, 13.75, and 3.21 ppm, respectively, in CD_2Cl_2 at 298 K. Later, the complex was characterized as

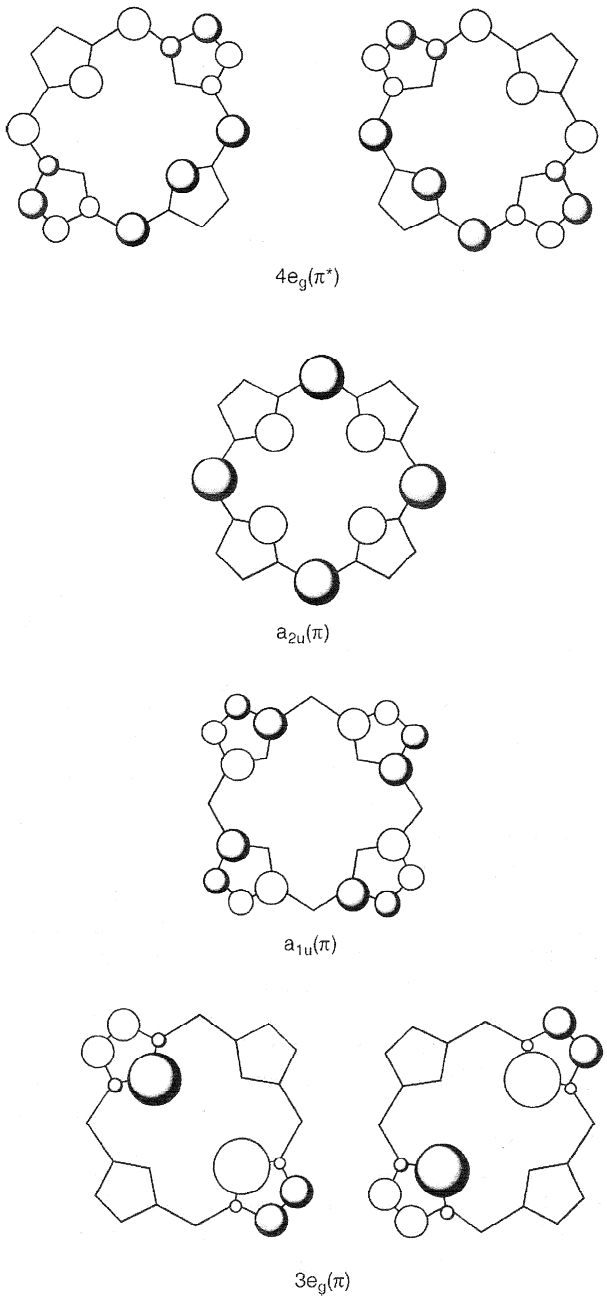

Fig. 4. Frontier orbitals of porphyrin.

the first example of the low-spin complex with the unusual $(d_{xz}, d_{yz})^4(d_{xy})^1$ electron configuration [31–33].

In the $(d_{xz}, d_{yz})^4(d_{xy})^1$ type complexes, the unpaired electron is in the d_{xy} orbital. Since the d_{xy} orbital is orthogonal to any of the porphyrin orbitals in the planar complexes with D_{4h} symmetry, the delocalization of the unpaired electron to the porphyrin ring is supposed to be quite small as far as the porphyrin maintains the planar structure. X-ray crystallographic studies of the $(d_{xz}, d_{yz})^4(d_{xy})^1$ type complexes have revealed, however, that the porphyrin core of these complexes commonly exhibits the highly ruffled structure [32,37–39]. Typical example is $[Fe(TPP)(4\text{-}CNPy)_2]ClO_4$ whose molecular structure is given in Fig. 5 [32].

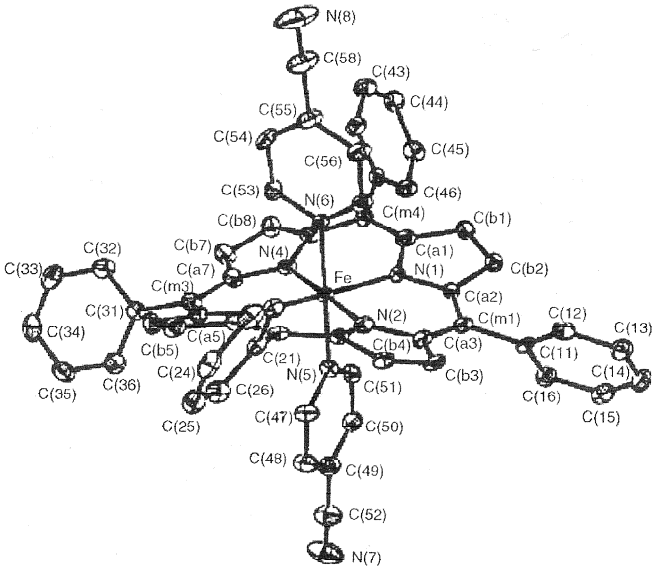

Fig. 5. ORTEP diagram of $[Fe(TPP)(4\text{-}CNPy)_2]ClO_4$. Labels assigned to the crystallographycally unique atoms are displayed. Fifty percent probability surfaces are shown. Adapted from Ref. [32].

The porphyrin ring is significantly ruffled. The equatorial Fe–N bond distances average to 1.952 Å, which is quite short for low-spin complex [40–42]. The average deviation of the *meso* carbon atoms from the mean porphyrin plane is 0.55 Å. Upon ruffling deformation, the symmetry of six-coordinate metalloporphyrin will be lowered from D_{4h} to D_{2d} [13–15]. As shown in Table 1 [14], both the iron d_{xy} and porphyrin a_{2u} orbitals are represented as b_2 in ruffled D_{2d} complex and therefore they can interact [32]. In other word, the complex is stabilized due to the d_{xy}–a_{2u} interaction by ruffling the porphyrin core. As a result, the unpaired electron in the d_{xy} orbital delocalizes to the porphyrin ring especially on the *meso* carbon and pyrrole nitrogen atoms because the a_{2u} orbital has large coefficients at these atoms as shown in Fig. 4. The upfield shift of the *o*- and *p*-H signals and the downfield shift of the *m*-H signal in the $(d_{xz}, d_{yz})^4(d_{xy})^1$ type complexes are therefore ascribed to the delocalization of the unpaired electron to the *meso* carbon atoms [4]. Small downfield isotropic shift of the pyrrole-H signal is explained in terms of the dipolar contribution since the contact shift is supposed

Table 1
Correlation table for the molecular orbitals of metalloporphyrin[a]

	D_{4h}	D_{2h}	D_{2d}	C_{4v}
Metal				
$d_{x^2-y^2}$	b_{1g}	a_g	b_2 (b_1)	b_1
d_{z^2}	a_{1g}	a_g	a_1	a_1
d_{zx}, d_{yz}	e_g	b_{2g}, b_{3g}	e	e
d_{xy}	b_{2g}	b_{1g}	b_1 (b_2)	b_2
Porphyrin				
LUMO	e_g	b_{2g}, b_{3g}	e	e
HOMO	a_{1u}	a_u	b_1	a_2
	a_{2u}	b_{1u}	b_2	a_1
HOMO-1	e_g	b_{2g}, b_{3g}	e	e

[a] Symmetry representation for ruffle-shaped deformation are given in parentheses. Adapted from Ref. [14].

Table 2
^{13}C NMR chemical shifts of $[Fe(TArP)(CN)_2]^-$ taken in CD_2Cl_2 and in CD_3OD, where Ar is 2,4,6-triethylphenyl group [44]

X	σ_p	CD_2Cl_2			CD_3CD		
		meso	α	β	*meso*	α	β
$-OCH_3$	−0.28	94.4	40.2	89.8	203.9	ca. 21	88.3
$-CH_3$	−0.14	93.5	40.3	89.9	195.8	22.4	88.6
−H	0.00	89.0	41.3	90.3	183.8	26.6	89.4
−F	0.15	84.2	42.4	90.6	173.2	30.7	90.2
−Cl	0.24	81.1	42.9	90.9	163.7	33.3	90.8
$-COOCH_3$	0.44	79.2	43.6	91.4	152.8	36.5	91.7
$-CF_3$	0.53	74.8	43.9	91.6	145.8	38.5	92.4
−CN	0.70	74.3	47.3	92.9	136.5	41.3	93.3

to be quite small due to the zero coefficients at the β-pyrrole carbons in the a_{2u} orbital [43].

In addition to the field strengths of axial ligands, electron configuration can also be affected by the electronic effect of the peripheral substituents. The ^1H and ^{13}C NMR data of a series of $[Fe(TArP)(CN)_2]^-$ are instructive, where Ar's are *p*-substituted phenyl groups [44]. Table 2 shows the ^{13}C NMR chemical shifts of these complexes taken in CD_2Cl_2 and CD_3OD solutions. The isotropic shift of the *meso* carbon in each complex, which is defined as $\delta_{iso} = \delta_{obs} - \delta_{dia}$, is plotted against the Hammett σ_p value, where δ_{dia} is the chemical shift of the *meso* carbon signal of the corresponding diamagnetic $[Co(TArP)(CN)_2]^-$. Fig. 6 shows the Hammett plots for the complexes obtained in (a) CD_2Cl_2 and (b) CD_3OD solutions. In CD_2Cl_2 solution, the Hammett plots yield a good linearity with a slope of −21.8 ppm. In

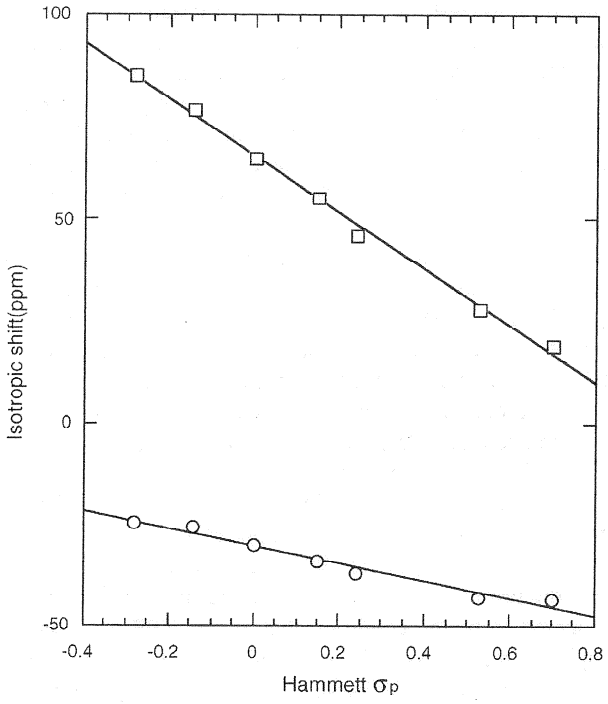

Fig. 6. Plots of the *meso* carbon isotropic shifts of $[Fe(TArP)(CN)_2]^-$ against Hammett σ_p. The symbols (○) and (□) are isotropic shifts obtained in CD_2Cl_2 and CD_3OD solutions, respectively. Adapted from Ref. [44].

CD_3OD solution, the Hammett plots again show a good linearity with a slope of −69.5 ppm, which is more than three times as much as that in CD_2Cl_2 solution. As mentioned later, the downfield shift of the *meso* carbon signal in low-spin complexes is a good measure to elucidate the contribution of the $(d_{xz}, d_{yz})^4(d_{xy})^1$ state. Thus, the results indicate that the contribution of the $(d_{xz}, d_{yz})^4(d_{xy})^1$ state is much larger in CD_3OD solution, and that it increases as the electron-donating ability of the *p*-substituents increases. Since the steric effect of the *p*-substituent on the porphyrin structure is considered to be negligibly small, it is concluded that the electron-donating *meso* substituent stabilizes the $(d_{xz}, d_{yz})^4(d_{xy})^1$ state while the electron-withdrawing substituent stabilizes the $(d_{xy})^2(d_{xz}, d_{yz})^3$ state [44].

2.2. Spectroscopic studies on the effect of porphyrin deformation

The complexes with the less common $(d_{xz}, d_{yz})^4(d_{xy})^1$ ground state exhibit a ruffled structure even if they have the usually planar porphyrin ring such as TPP, OEP, or TMP. Important problem here is if the reverse is true. Do the low-spin complexes carrying imidazole or cyanide exhibit the less common $(d_{xz}, d_{yz})^4(d_{xy})^1$ ground state if the complexes are forced to ruffle for steric reasons? In order to answer this question, Ikeue et al. have examined the electronic structures of a series of six-coordinate $[Fe(TRP)(L)_2]^+$, where R's are H, Me, Et, ^{n}Pr, ^{c}Pr, and ^{i}Pr groups [43,45–47] under the assumption that the ruffling of the porphyrin core is controlled by the bulkiness of *meso*-alkyl substituents [24–27]. In the following sections, the use of various spectroscopic methods such as ^{1}H NMR, ^{13}C NMR, and EPR to reveal the electronic ground state of low-spin iron(III) porphyrinates will be described [43,45–50].

2.2.1. ^{1}H NMR spectroscopy

Table 3 shows the chemical shifts of the pyrrole-H and *meso*-CH_α signals of $[Fe(TRP)(L)_2]^+$ [43,47], where axial ligands are nitrogen bases, CN^-, and ^{t}BuNC. The axial ligands are arranged in descending order of the CH_α chemical shifts, which almost coincides with the order of the pyrrole-H chemical shifts. The data in Table 3 clearly indicate that both the pyrrole-H and *meso*-CH_α signals move downfield in each series of $[Fe(TRP)(L)_2]^+$

Table 3
^{1}H NMR chemical shifts of $[Fe(TRP)L_2]^\pm$ in CD_2Cl_2 at 223 K

L	Py-H			*meso*-CHα		
	^{n}Pr	^{c}Pr	^{i}Pr	^{n}Pr	^{c}Pr	^{i}Pr
HIm	−21.5	−18.7	0.1	1.7	10.9	16.1
DMAP	−16.7	−14.3	4.0	9.7	26.4	19.8
2-MeIm	−8.2	−8.5	5.6	21.3	43.4	21.2
CN^-	−3.5	4.3	12.3	30.9	91.9	28.7
3-MePy	4.5	7.3	14.7	51.4	115.3	33.2
Py	7.1	8.4	14.9	57.9	121.4	34.0
4-CNPy	13.0	14.9	15.6	88.5	189.5	41.6
^{t}BuNC	12.7	14.7	12.9	118.5	[a]	50.8

Adapted from Refs. [43,47].
[a] Not observed.

as the field strength of the nitrogen base weakens, which in turn indicates that the electron configuration changes from $(d_{xy})^2(d_{xz}, d_{yz})^3$ to $(d_{xz}, d_{yz})^4(d_{xy})^1$.

Interestingly, the pyrrole-H signal also shows a downfield shift as the *meso* ^{n}Pr group is replaced by much bulkier ^{c}Pr, and then by ^{i}Pr group. Thus, it is reasonable to conclude that the contribution of the $(d_{xz}, d_{yz})^4(d_{xy})^1$ ground state increases as the ruffling of the porphyrin core increases. Although the molecular structures of these complexes have not been reported, the corresponding high-spin Fe(TRP)Cl actually exhibits the increase in ruffling as the *meso* substituent(R) changes from ^{n}Pr [51] to ^{c}Pr [52], and then to ^{i}Pr [53]. The ruffling dihedral angle, which is defined as the dihedral angle between two diagonal pyrrole rings, increases from 21.7° to 29.0°, and then to 38.2°. The average equatorial Fe–N bond decreases from 2.063 to 2.044, and then to 2.038 Å for the same change in the *meso* substituents. The short equatorial Fe-N bond is one of the characteristic features of the highly ruffled iron(III) porphyrin complexes. Latos-Grazynski, Marchon and others reported similar results using $[Fe(TMCP)L_2]^\pm$ and $[Fe(TCHP)L_2]^\pm$ having bulky cycloalkyl groups such as substituted cyclopropyl and cyclohexyl groups, respectively [48,49].

Another interesting datum in Table 3 is the difference in chemical shifts between $[Fe(TRP)(HIm)_2]^+$ and $[Fe(TRP)(2\text{-}MeIm)_2]^+$. Both the pyrrole-H and *meso*-CH_α signals exhibit large downfield shift as the axial ligand changes from HIm to much bulkier 2-MeIm. The result is again ascribed to the increase in the $(d_{xz}, d_{yz})^4(d_{xy})^1$ contribution due to the strongly ruffled porphyrin core in $[Fe(TRP)(2\text{-}MeIm)_2]^+$ caused by the steric repulsion between bulky 2-MeIm and the TRP core. In fact, the X-ray crystallographic analysis of analogous $[Fe(TEtP)(2\text{-}MeIm)_2]^+$ exhibits the presence of highly ruffled porphyrin core as shown in Fig. 7 [54]. The average deviation of the *meso* carbon atoms from the mean porphyrin plane reaches as much as 0.72 Å, indicating that the complex is one of the most severely ruffled low-spin iron(III) porphyrinates. The average equatorial Fe–N bond length is quite short 1.932 Å, which should be compared with 1.993 Å in analogous $[Fe(TPP)(HIm)_2]^+$ [55]. The short equatorial Fe–N bond is observed in $[Fe(TMP)(1,2\text{-}Me_2Im)_2]^+$, which also has strongly ruffled porphyrin core caused by the steric repulsion between bulky 1,2-Me_2Im and the TMP core [56]. The average equatorial bond length and the average deviation of the *meso* carbon atoms from the mean porphyrin plane are 1.937 and 0.72 Å, respectively. Thus, the degree of ruffling is nearly the same as that of $[Fe(TEtP)(2\text{-}MeIm)_2]^+$. Since the pyrrole-H chemical shifts of $[Fe(TEtP)(2\text{-}MeIm)_2]^+$ and $[Fe(TMP)(1,2\text{-}Me_2Im)_2]^+$ are −9.0 and −13.1 ppm, respectively, at 223 K [57], the *meso* ethyl group stabilizes the $(d_{xz}, d_{yz})^4(d_{xy})^1$ state more effectively than the *meso* mesityl group, which should be ascribed to the difference in electron donating ability between alkyl and aryl groups. Probably, 2-MeBzIm is the bulkiest imidazole ligand that can coordinate to iron(III) porphyrinates. Thus, the low-spin $[Fe(TMP)(2\text{-}MeBzIm)_2]^+$ is expected to show the most severely ruffled porphyrin core though the structural data are not available at present. The pyrrole-H of $[Fe(TMP)(2\text{-}MeBzIm)_2]^+$ shows four signals around +1 ppm at 223 K, suggesting that

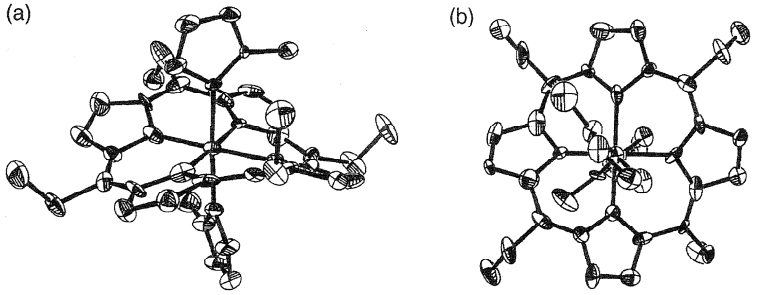

Fig. 7. ORTEP diagram of [Fe(TEtP)(2-MeIm)$_2$]Cl: (a) side view and (b) top view. Adapted from Ref. [54].

the complex adopts the $(d_{xz}, d_{yz})^4(d_{xy})^1$ ground state in spite of the coordination of imidazole derivative [58]. Determination of the electronic ground state of analogous low-spin [Fe(TPP)(2-MeBzIm)$_2$]$^+$ has been hampered due to the facile formation of the μ-oxo dimer in the presence of hindered base [59].

The difference in electron configuration in low-spin complexes should affect the chemical shifts of the axial ligands. If the coordination atom in the axial ligand constitutes a part of double or triple bond as in the case of imidazoles, pyridines, or cyanide, the d_π–p_π or d_π–$p_{\pi*}$ interaction is possible in the $(d_{xy})^2(d_{xz}, d_{yz})^3$ type complexes. As a result, we can expect the presence of isotropically shifted ligand signals. In contrast, the isotropic shift must be much smaller in the $(d_{xz}, d_{yz})^4(d_{xy})^1$ type complexes since the d_{xy} orbital is orthogonal to any of the ligand π orbitals. Thus, the chemical shift of the axial ligands can also be a good probe to elucidate the electron configuration. Fig. 8 shows the correlation of the chemical shifts between pyrrole and imidazole methyl protons in [Fe(TRP)(2-MeIm)$_2$]$^+$ (**1a–1d**) and [Fe(TRP)(2-MeIm)(CN)] (**2a–2d**), where R = H(a), Me(b), Et(c), and ^{i}Pr(d) [46]. As the pyrrole signal moves downfield from −22.5 in [Fe(THP)(2-MeIm)$_2$]$^+$ (**1a**) to 12.4 ppm in [Fe(T^{i}PrP)(2-MeIm)(CN)] (**2d**), the imidazole methyl signal shifts upfield from 21.4 to −6.0 ppm. The results indicate that the spin density at the C-2 of the coordinated 2-MeIm ligand decreases in both systems on going from R = H to R = ^{i}Pr, which in turn indicates the switch of the electron configuration from $(d_{xy})^2(d_{xz}, d_{yz})^3$ to $(d_{xz}, d_{yz})^4(d_{xy})^1$ [46]. The dipolar shift also contributes to some extent because the methyl signal is expected to move upfield in the $(d_{xz}, d_{yz})^4(d_{xy})^1$ type, and downfield in the $(d_{xz}, d_{yz})^4(d_{xy})^1$ complexes [43]. In Fig. 8, the complexes (**1d**) and (**2b–2d**), all of which are located at lower right of the graph, are confirmed to adopt the $(d_{xz}, d_{yz})^4(d_{xy})^1$ ground state on the basis of the EPR *g* values [46].

2.2.2. ^{13}C NMR spectra

^{13}C NMR chemical shift is also a good probe to elucidate the electronic structure of the low spin complexes [43,45–47,60–64]. The isotropic shifts (δ_{iso}) of the carbon signals are given by

$$\delta_{iso} = \delta_{obs} - \delta_{dia} = \delta_{dip}^{MC} + \delta_{dip}^{LC} + \delta_{con}$$

where δ_{dip}^{MC}, δ_{dip}^{LC}, and δ_{con} represent the metal centered dipolar shift, ligand centered dipolar shift, and contact shift, respectively. The metal centered dipolar shift in the complexes with axial symmetry is defined as follows:

$$\delta_{dip}^{MC} = \frac{1}{12\pi}(\chi_{||} - \chi_{\perp})\frac{3\cos^2\theta - 1}{r^3}$$

where χ's are the molecular susceptibilities, θ the angle between the nucleus–metal vector and the *z*-axis, *r* the length of this vector, and term $(3\cos^2\theta - 1)/r^3$ is referred to as the axial geometric factor. The δ_{dip}^{LC} is assumed to be proportional to the spin density ρ^π at the observed carbon atom and is given by

$$\delta_{dip}^{LC} = D\rho^\pi$$

Carbon contact shifts originate from unpairing of carbon 1s electrons and unpairing of the three carbon sp^2 bonding pairs. Thus, the contact shift for the *meso* carbon in [Fe(TRP)L$_2$]$^\pm$ can be written by the Karplus and Frankel equation [65], where

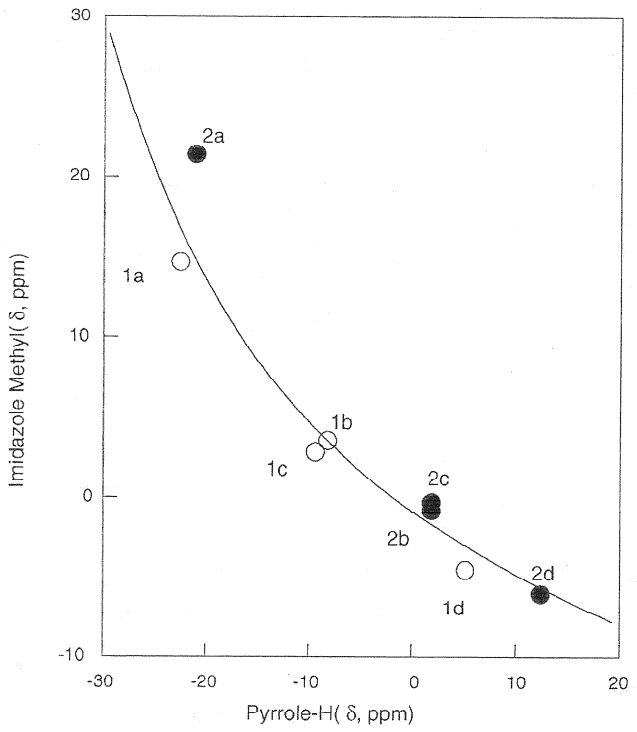

Fig. 8. Correlation of the chemical shifts between pyrrole-H and imidazole methyl signals in a series of [Fe(TRP)(2-MeIm)$_2$]$^+$ (○) (**1a–1d**) and [Fe(TRP)(2-MeIm)(CN)] (●) (**2a–2d**)at 238 K, where R = H(a), Me(b), Et(c), and ^{i}Pr(d). The line has no mathematical meaning. Adapted from Ref. [46].

$F^C = \{2\pi g\mu_B S(S+1)\}/(3\gamma_C kT)$:

$$\delta_{con}(meso) = [(S^C + 3Q^C_{CC'})\rho^\pi_{meso} + (2Q^C)\rho^\pi_\alpha]F^C$$

The S^C term indicates polarization of the 1s orbital, the $Q^C_{CC'}$ term reflects polarization of the three sp^2 bonds by π-spin density at the observed carbon atom, and the $Q^C_{C'C}$ term represents polarization of the C–C bond by π spin densities centered on the neighboring carbon atoms. The S^C, $Q^C_{CC'}$, and $Q^C_{C'C}$ are estimated to be −35.5, 40.3, and −39.0 MHz, respectively [65,66]. The $(\delta_{con} + \delta^{LC}_{dip})$ values for the *meso* carbon, which can be obtained by $(\delta_{iso} - \delta^{MC}_{dip})$, are expressed by

$$\delta_{con} + \delta^{LC}_{dip} = \delta_{iso} - \delta^{MC}_{dip} = [(S^C + 3Q^C_{CC'})\rho^\pi_{meso} + 2Q^C_{C'C}\rho^\pi_\alpha]F^C + D\rho^\pi_{meso}$$

The *meso*-^{13}C chemical shift is particularly useful to determine the electron configuration [43,47,67]. This is because the spin densities on the *meso* carbon atoms are quite dependent on the electron configuration. The $3e_g$ orbital, which interacts with the half-occupied d_π orbital in the $(d_{xy})^2(d_{xz}, d_{yz})^3$ type complexes, has node at the *meso* carbon atom. Thus, the *meso* carbon isotropic shift, $\delta_{iso}(meso)$, is approximated by Eq. (1) assuming that the ρ^π_{meso} is negligibly small:

$$\delta_{iso}(meso) = 2Q^C_{C'C}F^C\rho^\pi_\alpha + \delta^{MC}_{dip} \quad (1)$$

Since both terms in Eq. (1) are negative, the *meso* signal appears more upfield than the corresponding signal in diamagnetic complexes; δ^{MC}_{dip} is negative because of the positive $(\chi_{||} - \chi_\perp)$ value in the $(d_{xy})^2(d_{xz}, d_{yz})^3$ type complexes. By contrast, the complexes with the $(d_{xz}, d_{yz})^4(d_{xy})^1$ ground state have large spin density at the *meso* and negligibly small spin density at the α carbon atoms due to the a_{2u}–d_{xy} interaction. Thus, the *meso* carbon isotropic shift for the $(d_{xz}, d_{yz})^4(d_{xy})^1$ type complexes is approximated by Eq. (2) assuming that the ρ^π_α is negligibly small:

$$\delta_{iso}(meso) = [D + (S^C + 3Q^C_{CC'})F^C]\rho^\pi_{meso} + \delta^{MC}_{dip} \quad (2)$$

Since the D, $(S^C + 3Q^C_{CC'})$, and δ^{MC}_{dip} values are all positive, the *meso* carbon isotropic shift is positive and increases linearly with the π spin density at the *meso* carbon; δ^{MC}_{dip} is positive because $(\chi_{||} - \chi_\perp)$ is negative in the $(d_{xz}, d_{yz})^4(d_{xy})^1$ type complexes. Thus, the complex with a quite pure $(d_{xz}, d_{yz})^4(d_{xy})^1$ ground state with a highly ruffled porphyrin core should exhibit the *meso* carbon signal at a fairly downfield position due to the strong d_{xy}–a_{2u} interaction.

The ^{13}C NMR chemical shifts of the *meso*, α, and β signals of a series of $[Fe(TRP)L_2]^\pm$ are listed in Table 4 [43,47]. The data indicate that the *meso* signal moves downfield as the axial ligand has much weaker σ-donating and stronger π-accepting ability; the chemical shifts of the *meso* signals in $[Fe(T^nPrP)L_2]^+$ are 73.1 and 814.7 ppm for L = HIm and 4-CNPy, respectively. The data in Table 4 also indicate that the $(d_{xz}, d_{yz})^4(d_{xy})^1$ character increases with increasing bulkiness of the *meso* alkyl group; the *meso* carbon signals in $[Fe(TRP)(HIm)_2]^+$ are 73.1, 97.1, and 331.6 ppm for R = ^{n}Pr, ^{c}Pr, and ^{i}Pr, respectively. Thus, the chemical shift of *meso* carbon is as good a probe as that of pyrrole-H in determining the electron configuration of the low spin complexes. Since the *meso* carbon chemical shifts of the corresponding diamagnetic complexes $[Co(TRP)L_2]^+$ are ca. 125 ppm, it is clear from Eqs. (1) and (2) that the ground state electron configuration of $[Fe(T^nPrP)(HIm)_2]^+$ is different from that of $[Fe(T^iPrP)(HIm)_2]^+$; the former adopts the $(d_{xy})^2(d_{xz}, d_{yz})^3$ while the latter adopts the $(d_{xz}, d_{yz})^4(d_{xy})^1$ electron configuration. Highly ruffled complex carrying the axial ligand with low-lying π^* orbital, i.e. $[Fe(T^iPrP)(4\text{-}CNPy)_2]^+$, shows the *meso* signal at an extremely downfield position, 917.5 ppm at 223 K, indicating that the complex is in a quite pure $(d_{xz}, d_{yz})^4(d_{xy})^1$ ground state. The complex with the purest $(d_{xz}, d_{yz})^4(d_{xy})^1$ ground state, where the d_{xy} orbital is located far above the d_π orbitals, must be $[Fe(T^iPrP)(^tBuNC)_2]^+$ as is revealed from the extraordinary downfield shifted CH_α signal shown in Table 3 [47]. Observation of the *meso* signal of this complex is, however, not successful at this point.

As mentioned, the characteristic NMR features in the $(d_{xz}, d_{yz})^4(d_{xy})^1$ type complexes are the downfield shift of the *meso*-^{13}C and the downfield shift of the pyrrole-H signals. Fig. 9 shows the correlation between pyrrole-H and *meso*-^{13}C chemical shifts of a series of $Fe(TRP)L_2^+$ (R = ^{n}Pr, ^{c}Pr, and ^{i}Pr) and $Fe(TArP)L_2^+$ (Ar = phenyl and mesityl groups) determined in CD_2Cl_2 solution at 298 K [67]. As the $(d_{xz}, d_{yz})^4(d_{xy})^1$ character increases, both the pyrrole-H and *meso*-^{13}C signals move downfield, showing a semi-parabolic curve with a positive slope.

Table 4
^{13}C NMR chemical shifts of low-spin $Fe(TRP)L_2^+$ in CD_2Cl_2 at 223 K

L	*meso*			α			β		
	^{n}Pr	^{c}Pr	^{i}Pr	^{n}Pr	^{c}Pr	^{i}Pr	^{n}Pr	^{c}Pr	^{i}Pr
HIm	73.1	97.1	331.6	0.0	11.8	−28.3	73.6	79.6	76.5
DMAP	130.5	127.4	402.2	−2.2	8.5	−47.2	84.3	88.0	81.1
2-MeIm	n.d.	190.4	434.0	n.d.	−20.6	−69.9	n.d.	n.d.	74.8
CN^-	336.1	386.7	639.6	−72.7	−84.2	−186.0	61.2	61.2	54.7
3-MePy	470.0	431.6	702.5	−88.5	−71.1	−165.2	77.0	79.6	71.6
Py	526.5	448.9	728.6	−108.2	−81.3	−179.3	74.3	78.7	71.4
4-CNPy	814.7	680.1	917.5	−267.2	−211.9	−293.5	66.0	71.7	74.8
^{t}BuNC	[a]	[a]	[a]	[a]	[a]	[a]	84.7	91.0	98.8

Adapted from Ref. [43,47].
[a] Not observed.

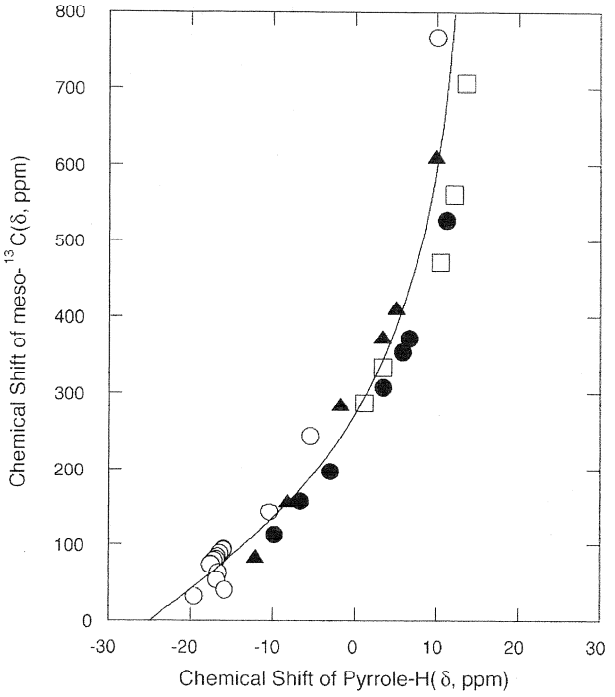

Fig. 9. Corelation of chemical shifts between pyrrole-H and *meso*-^{13}C signals at 298 K in $[Fe(TArP)L_2]^{\pm}$ (○), $[Fe(T^nPrP)L_2]^{\pm}$ (▲), $[Fe(T^cPrP)L_2]^{\pm}$ (●), and $[Fe(T^iPrP)L_2]^{\pm}$ (□). The line has no mathematical meaning. Adapted from Ref. [67].

The correlation curve is quite useful to elucidate the contribution of the $(d_{xz}, d_{yz})^4(d_{xy})^1$ in naturally occurring heme proteins since the hemes have no pyrrole-H.

The ^{13}C NMR chemical shift of iron-bound cyanide can also be a probe to elucidate the electronic structure of iron(III) porphyrinates and naturally occurring heme proteins [6,68]. The iron-bound cyanide signals are observed fairly upfield, ca. −2500 ppm, mainly due to the contact shift caused by the spin polarization effect; the unpaired electron in iron polarizes the Fe–C σ-bond and induces the negative spin at the CN carbon atom [69]. Since the cyanide chemical shift is affected by various factors including solvents, hydrogen bonding, trans ligand, etc., it must be difficult to extract the effect of electron configuration from the observed chemical shifts [70]. In the case of $[Fe(TRP)(CN)_2]$, the cyanide signal moves downfield as the electron configuration switches from $(d_{xy})^2(d_{xz}, d_{yz})^3$ to $(d_{xz}, d_{yz})^4(d_{xy})^1$; they are −2973 ppm (H), −1840 ppm (Me), −2054 ppm (Et), and −1530 ppm (^{i}Pr) in CD_2Cl_2 at 248 K [45].

Once the ^{1}H and ^{13}C NMR chemical shifts are determined, it is possible to calculate the spin densities on the porphyrin carbon and nitrogen atoms. Fig. 10 shows the spin distribution in low-spin $[Fe(TPP)(1\text{-}MeIm)_2]^+$ and $[Fe(T^iPrP)(4\text{-}CNPy)_2]^+$, which adopt the $(d_{xy})^2(d_{xz}, d_{yz})^3$ and $(d_{xz}, d_{yz})^4(d_{xy})^1$ ground state, respectively. In the case of $[Fe(TPP)(1\text{-}MeIm)_2]^+$, the unpaired electron delocalizes from the iron d_π orbital to the pyrrole nitrogen and β carbon atoms [63]. In contrast, a large amount of spin is on the pyrrole nitrogen and *meso* carbon atoms in $[Fe(T^iPrP)(4\text{-}CNPy)_2]^+$ [43]. The total spin delocalized to the porphyrin ring reaches as much as 0.48 in $[Fe(T^iPrP)(4\text{-}CNPy)_2]^+$, while it is

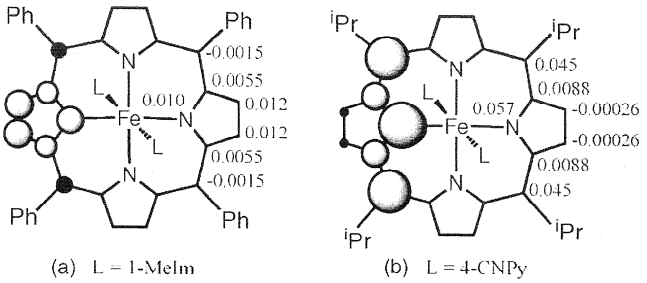

Fig. 10. Spin distribution in low-spin (a) $[Fe(TPP)(1\text{-}MeIm)_2]^+$ and (b) $[Fe(T^iPrP)(4\text{-}CNPy)_2]^+$. Adapted from Ref. [43].

only 0.17 in $[Fe(TPP)(1\text{-}MeIm)_2]^+$. Thus, the porphyrin ring in $[Fe(T^iPrP)(4\text{-}CNPy)_2]^+$ has significant a_{2u} type radical character due to the strong a_{2u}–d_{xy} interaction [43], which is supported by the theoretical calculation [71].

2.2.3. EPR spectra

EPR spectroscopy is a good method to elucidate the electron configuration of the low spin complexes at an extremely low temperature [3–5,72–74]. The complexes with the $(d_{xz}, d_{yz})^4(d_{xy})^1$ ground state exhibit axial type spectra where g_{xx} and g_{yy} are nearly the same and they are larger than g_{zz}. The complexes with the $(d_{xy})^2(d_{xz}, d_{yz})^3$ ground state show either rhombic or "large g_{max}" type spectra. Extensive studies by Walker, Scheidt et al. have revealed that the relative orientation of planar axial ligands determines the spectral type of the low-spin complexes [5,75]. Complexes carrying parallel aligned ligands exhibit the rhombic type spectra, where three signals are observed at $g_1 = 1.5$–1.9, $g_2 = 2.2$–2.4, and $g_3 = 2.5$–2.9. In contrast, the complexes carrying perpendicularly aligned ligands give large g_{max} type spectra, where a single strong signal appears at $g = 3.2$–3.7. The complexes with linear ligands such as cyanide also exhibit the large g_{max} type spectra. It is possible that the low-spin complex has two isomers with different ligand orientation; one has parallel aligned and the other has perpendicularly aligned ligands. In such a case, both rhombic and large g_{max} type signals can be observed even in frozen solution if the interconversion is slow on the EPR timescale. Fig. 11 shows the EPR spectra of the DMAP complexes taken in frozen CH_2Cl_2 solution at 4.2 K [76]. As shown in Fig. 11(b), $[Fe(OEP)(DMAP)_2]^+$ gives a typical rhombic spectrum with three signals at $g = 2.81$, 2.38, and 1.64, suggesting that the two DMAP molecules take a mutually parallel orientation above and below the porphyrin ring in frozen CH_2Cl_2 solution. The parallel alignment of the two DMAP ligands is confirmed in the solid by the X-ray crystallographic analysis [75]. By contrast, $[Fe(OETPP)(DMAP)_2]^+$ exhibits a large g_{max} type signal at $g = 3.24$ as shown in Fig. 11(c). The result suggests that the two DMAP molecules are aligned perpendicularly in frozen CH_2Cl_2 solution at 4.2 K. Structural analyses of this complex reveal that the dihedral angle between two axial ligands is 53.2° in one report [77] and 70° in another report [78]. In the case of $[Fe(TMTMP)(DMAP)_2]^+$, both rhombic and large g_{max} signals coexist as shown in Fig. 11(a), which indicates the existence of two isomers with different ligand orientation. If the equilibrium constant between two isomers is ca. 10 in favor of the perpendicular isomer, the ΔG° is calculated to be

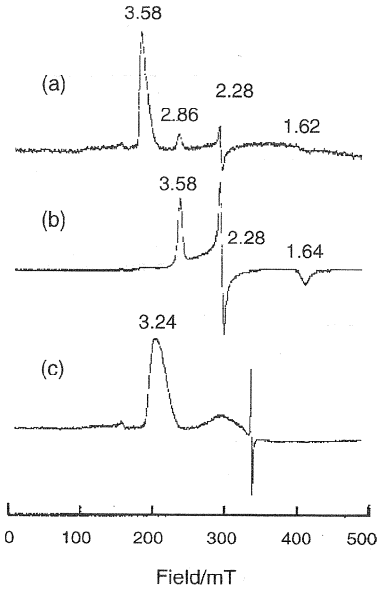

Fig. 11. EPR spectra of (a) $[Fe(TMTMP)(DMAP)_2]^+$, (b) $[Fe(OEP)(DMAP)_2]^+$, and (c) $[Fe(OETPP)(DMAP)_2]^+$ taken in frozen CH_2Cl_2 solution at 4.2 K. Adapted from Ref. [76].

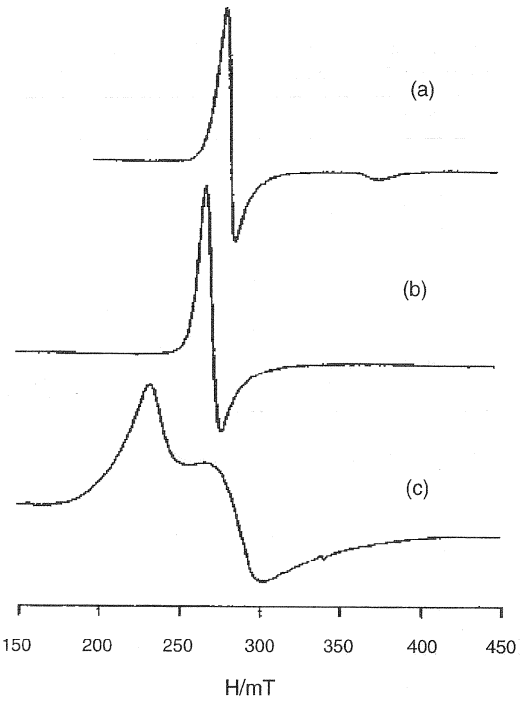

Fig. 12. EPR spectra of (a) $[Fe(T^iPrP)(4\text{-}CNPy)_2]^+$, (b) $[Fe(T^cPrP)(Py)_2]^+$, and $[Fe(T^nPrP)(HIm)_2]^+$taken in frozen CH_2Cl_2 solution at 4.2 K. Adapted from Ref. [47].

80 J/mol at 4.2 K. Thus, this phenomenon is observable when the difference in thermodynamic stability of the isomers is fairly small. More recently, Walker et al. reported the formation of two isomeric $[Fe(OMTPP)(1\text{-}MeIm)_2]Cl$ with different ligand orientation [79]. One is paral-$[Fe(OMTPP)(1\text{-}MeIm)_2]Cl$ and the other is perp-$[Fe(OMTPP)(1\text{-}MeIm)_2]Cl$, where the dihedral angles of the ligands are 19.5° and 90.0°, respectively. In the solid, the former exhibits a rhombic signal with $g_1 = 1.54$, $g_2 = 2.51$, and $g_3 = 2.71$, while the latter shows a large g_{max} signal at $g = 3.61$. It has been proposed that the spectral switch from the large g_{max} type to the rhombic type EPR signal takes place when the dihedral angles between two axial planar ligands are in the range of 30–70° [79].

Fig. 12 shows the EPR spectra of (a) $[Fe(T^iPrP)(4\text{-}CNPy)_2]^+$, (b) $[Fe(T^cPrP)(Py)_2]^+$, and (c) $[Fe(T^nPrP)(HIm)_2]^+$ taken in frozen CH_2Cl_2 solution at 4.2 K. As expected, $[Fe(T^iPrP)(4\text{-}CNPy)_2]^+$ and $[Fe(T^cPrP)(Py)_2]^+$ with a ruffled porphyrin core exhibit the axial type spectra. The $g_\perp$ and $g_{||}$ values are 2.41 and 1.79 for the former, and 2.56 and (1.3) for the latter complexes [43]; the value in parenthesis is a speculated one. A slightly smaller $g_\perp$ value in $[Fe(T^iPrP)(4\text{-}CNPy)_2]^+$ indicates that the energy gap between the d_{xy} and d_π orbitals is larger in $[Fe(T^iPrP)(4\text{-}CNPy)_2]^+$ than in $[Fe(T^cPrP)(Py)_2]^+$. In contrast to these spectra, $[Fe(T^nPrP)(HIm)_2]^+$ shows the rhombic type spectrum with $g_1 = 2.90$, $g_2 = 2.35$, $g_3 = (1.45)$. Thus, the complex adopts the $(d_{xy})^2(d_{xz}, d_{yz})^3$ ground state with parallel aligned imidazole ligands [47].

2.3. Electron configurational isomers

In principle, a low spin complex should adopt either the $(d_{xz}, d_{yz})^4(d_{xy})^1$ or the $(d_{xy})^2(d_{xz}, d_{yz})^3$ ground state depending on the d orbital ordering determined by the electronic nature of axial ligands, deformation of porphyrin ring, electronic effects of peripheral substituents, interaction with the solvent molecules, etc. It is possible, however, that a complex exists as the equilibrium mixture of the two isomers with different electronic ground states; one has the $(d_{xz}, d_{yz})^4(d_{xy})^1$ ground state while the other has the $(d_{xy})^2(d_{xz}, d_{yz})^3$ ground state as shown in Eq. (3). Here, we define the *electron configurational isomers*, which indicate that the isomers adopting the same spin state differ in electron configuration.

$$(d_{xz}, d_{yz})^4(d_{xy})^1 \rightleftarrows (d_{xy})^2(d_{xz}, d_{yz})^3 \quad (3)$$

It must be very difficult, however, to directly observe the entities of such isomers because of the low energy barrier separating the isomers. In addition, two isomers must exist in a comparable ratio at an extremely low temperature for the direct observation. One possible way to find such complexes is to finely modulate the electronic nature of the axial ligands by means of intermolecular interactions with solvent molecules so that the two isomers exist in a comparable ratio at an extremely low temperature. Ikezaki and Nakamura [80] found that $[Fe(TArP)(CN)_2]^-$ meets the requirements if Ar is 2,4,6-triethylphenyl. The contribution of the $(d_{xz}, d_{yz})^4(d_{xy})^1$ electron configuration in this complex changes depending on the nature of the solvents used. Table 5 shows the ^{13}C NMR shifts of $[Fe(TArP)(CN)_2]^-$ taken in various solvents at 253 K. In general, the isotropic shifts of the *meso*-^{13}C signals are negative (upfield shift) in the complexes with the $(d_{xy})^2(d_{xz}, d_{yz})^3$ ground state as shown in Eq. (1), while they are positive (downfield shift) in the complexes with the $(d_{xz}, d_{yz})^4(d_{xy})^1$ ground state as shown in Eq. (2). Thus, the electronic ground state can be deduced on the basis of the signs of the *meso*

Table 5
^{13}C NMR chemical shifts of $[Fe(TArP)(CN)_2]^-$ determined in various solvents at 253 K, where Ar is 2,4,6-triethylphenyl

Solvents	*meso*	α	β	*ipso*	*o*	*m*	*p*
CD_3OD	275.4	−17.0	76.6	68.8	236.5	130.0	146.5
$CDCl_3$	191.4	9.3	76.2	91.8	202.0	125.6	142.5
CD_2Cl_2	172.3	10.4	78.5	97.0	193.2	125.3	143.1
DMF-d_7	134.9	18.6	78.0	106.9	178.4	125.0	143.1
DMSO-d_6[a]	130.8	16.2	78.5	107.0	176.4	124.5	142.4
$(CD_3)_2CO$	123.3	20.7	77.2	109.9	174.2	124.4	142.6
CD_3CN	100.3	20.4	81.1	113.4	165.1	123.4	142.6
$C_6D_5CD_3$	96.1	25.2	80.3	116.7	164.9	123.9	142.2
C_6D_6[a]	95.5	23.8	79.6	116.1	164.5	123.7	142.1
CCl_4	79.6	25.6	82.2	119.1	158.2	122.6	140.8

Adapted from Ref. [80].
[a] The value is extrapolated from high temperature.

carbon isotropic shifts; $\delta_{iso} = \delta_{obs} - \delta_{dia}$. Since the *meso* carbon shifts of diamagnetic $[Co(TArP)(CN)_2]^-$ are 115.5 ± 0.6 ppm in the solvents listed in Table 5, the border line that separates the $(d_{xz}, d_{yz})^4(d_{xy})^1$ type from the $(d_{xy})^2(d_{xz}, d_{yz})^3$ type complex lies between acetone and acetonitrile. In other words, the isomer with the $(d_{xz}, d_{yz})^4(d_{xy})^1$ ground state predominates over that with the $(d_{xy})^2(d_{xz}, d_{yz})^3$ ground state in the solvents ranging from methanol to acetone.

To directly observe the electron configurational isomers, spectroscopic measurement at an extremely low temperature is necessary. Fig. 13 shows the EPR spectra of $[Fc(TArP)(CN)_2]^-$ taken in a series of frozen solutions at 4.2 K. In consistent with the ^{13}C NMR results, the complex exhibits the axial type spectrum in the solvents ranging from methanol to acetone. However, in the solvents that stabilizes the $(d_{xy})^2(d_{xz}, d_{yz})^3$ ground state such as acetonitrile, toluene, and benzene, the EPR spectra exhibit both large g_{max} and axial type signals. The result strongly indicates that two isomers with the different ground states actually exist in frozen solution at 4.2 K and that the mutual exchange between these two isomers is slow on the EPR time scale at this temperature. Since the complexes with the $(d_{xz}, d_{yz})^4(d_{xy})^1$ ground state always exhibit the ruffled porphyrin ring in $[Fe(TRP)L_2]^+$ and $[Fe(TArP)L_2]^+$, the observation of the two isomers is ascribed to the slow interconversion between the ruffled complex with the $(d_{xz}, d_{yz})^4(d_{xy})^1$ ground state and, possibly, the planar (or nearly planar) complex with the $(d_{xy})^2(d_{xz}, d_{yz})^3$ ground state as shown in Fig. 14. Rivera et al. also proposed

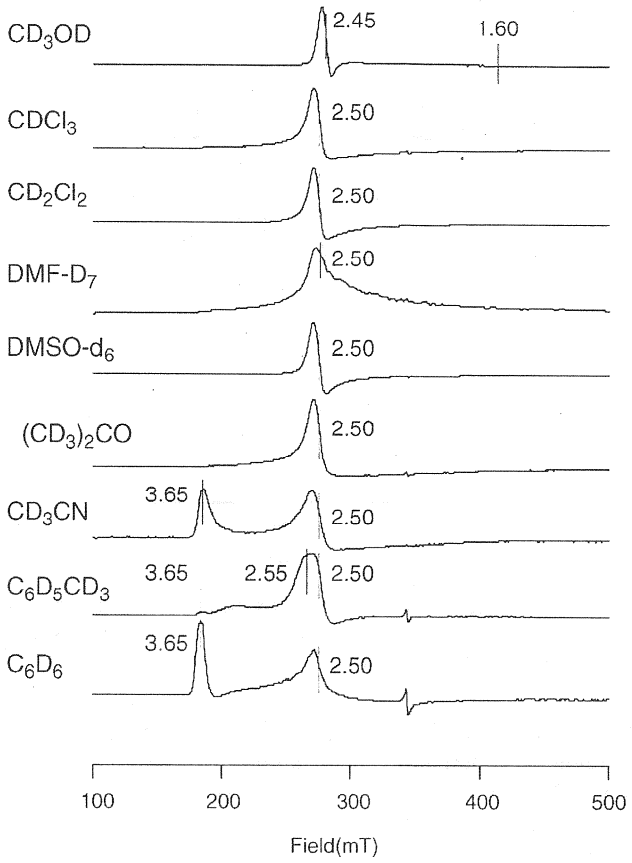

Fig. 13. EPR spectra of $[Fe(TArP)(CN)_2]^-$ taken in frozen solutions at 4.2 K, where Ar is 2,4,6-triethylphenyl. Adapted from Ref. [80].

the presence of the equilibrium between the planar $(d_{xy})^2(d_{xz}, d_{yz})^3$ and ruffled $(d_{xz}, d_{yz})^4(d_{xy})^1$ to explain the Curie plots of the *meso* signal in $[Fe(TPP)(OCH_3)(OO^tBu)]^-$ [81,82].

3. Mixed high-spin and intermediate-spin state

3.1. General Consideration

Five-coordinate iron(III) porphyrin complexes with anionic axial ligands such as chloride and acetate usually show the high-spin ($S = 5/2$) state [40–42]. This is because the iron(III) ion deviates from the porphyrin plane in these complexes to stabi-

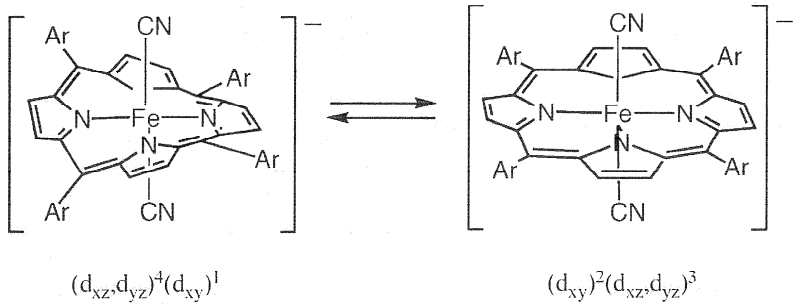

$(d_{xz},d_{yz})^4(d_{xy})^1$ $(d_{xy})^2(d_{xz},d_{yz})^3$

Fig. 14. Interconversion between the ruffled isomer with the $(d_{xz}, d_{yz})^4(d_{xy})^1$ ground state and the planar or nearly planar isomer with the $(d_{xy})^2(d_{xz}, d_{yz})^3$ ground state. Adapted from Ref. [80].

lize the $d_{x^2-y^2}$ orbitals [40–42]. If the axial chloride or acetate is replaced by a fairly weak anionic ligand, then the d_{z^2} orbital is stabilized and the $d_{x^2-y^2}$ orbital is destabilized. The destabilization of the $d_{x^2-y^2}$ orbital is ascribed to the interaction with the nitrogen lone pair; the interaction is strengthened due to the decrease in the out-of-plane distance of iron. As a result, the complex is expected to adopt an intermediate-spin ($S = 3/2$) state. Actually however, the complex with weak axial ligand shows not a pure $S = 3/2$ but a mixed $S = 3/2$, 5/2 spin state. The mixed spin state is considered to be a quantum mechanical admixture caused by the spin–orbit coupling between the high- and intermediate-spin states, and not a thermal equilibrium between two spin states [83,84]. In fact, no clear example has ever been reported even at very low temperatures to show the presence of the two species.

^{1}H NMR spectroscopy is a good method to determine the contribution of the $S = 3/2$ in the mixed spin state [3–8,85]. This is because the pure high-spin complex exhibits the pyrrole-H signal fairly downfield because of the presence of unpaired electron at the $d_{x^2-y^2}$ orbital; the unpaired electron in this orbital delocalizes to the pyrrole-H position through σ bonds and induces the large downfield shift of the pyrrole-H signal. In contrast, the $d_{x^2-y^2}$ orbital is depopulated in the pure intermediate-spin complexes. Thus, the pyrrole-H signal should appear fairly upfield due to the spin polarization effect caused by the unpaired electron at the β carbon atoms. On the basis of the pyrrole-H chemical shifts, Reed and Guiset succeeded in ranking the weakness of anionic ligands (X) in five-coordinate Fe(TPP)X and called the hierarchy given in Eq. (4) as magnetochemical series [86,87]. The weakest anionic ligand is determined to be $[Ag(Br_6CB_{11}H_6)_2]^-$ since the pyrrole-H signal is observed at the most upfield position:

$$[Ag(Br_6CB_{11}H_6)_2]^- < CB_{11}H_{12}^- < SbF_6^- < Co(C_2B_9H_{11})_2^- < AsF_6^- < ClO_4^- < C(CN)_3^- < CF_3SO_3^- < BF_4^- < ONC(CN)_2^- < ReO_4^- < OTeF_3^- < I^- < Br^- < Cl^- \quad (4)$$

The magnetochemical series is also applicable to porphyrin isomers such as porphycene [88–90]. The pyrrole signal of (TPrPc)FeX moves upfield as the axial ligand (X) changes from PhO^-, Cl^-, Br^-, I^-, and then to ClO_4^-, which corresponds to the spin state change from $S = 5/2$ to $S = 3/2$ [88].

The six-coordinate iron(III) complexes with nitrogen bases usually show the low-spin state. However, the complex can adopt a rare high-spin state if the oxygen containing neutral compound such as DMSO is used [91]. As in the case of the five-coordinate complexes, the high-spin state is converted to the intermediate-spin state if the field strength of the oxygen ligand is weakened. Table 6 lists the ^{1}H and ^{13}C NMR chemical shifts as well as EPR g values of a series of $Fe(TPP)L_2^+$ where L's are oxygen ligands [92,93]. The pyrrole-H signal moves upfield from 71 to 3 ppm as the axial ligand changes from 4-MePyNO to THF, indicating the increase in the $S = 3/2$ contribution. In Table 6, the axial ligands are arranged in descending order of the pyrrole-H chemical shifts, which therefore corresponds to the magnetochemical series for oxygen ligands. The order of the field strengths of some ligands such as PyNO, substituted PyNO's, and DMSO are difficult to determine from the data in Table 6 because of the similarity of the chemical shifts. The magnetochemical series shown in Eq. (5) has been determined on the basis of the pyrrole-H chemical shifts of both planar $[Fe(TPP)L_2]^+$ and ruffled $[Fe(T^iPrP)L_2]^+$ which will be mentioned later [92,93].

$$\text{4-MePyNO, 3, 5-Me}_2\text{PyNO} > \text{PyNO} > \text{4-ClPyNO} > \text{DMSO} > \text{DMF} > \text{MeOH} > \text{Et}_2\text{NNO} > \text{THF} \quad (5)$$

Although there is no example showing an essentially pure intermediate-spin state in $[Fe(TPP)L_2]^+$, the analogous $[Fe(TArP)(THF)_2]^+$ reported by Gold et al., where Ar is 2,4,6-trimethoxyphenyl, is in a quite pure intermediate-spin state on the basis of the spectroscopic and magnetic data [94–96]: ^{1}H NMR ($CDCl_3$, room temp, δ), −28.0 (Py-H), 9.2 (*m*-H); EPR ($CHCl_3$, 77 K) $g_\perp = 4.2$, $g_{||} = 2.0$; $\mu_{eff} = 4.7\ \mu_B$. Since the chemical shift of the pyrrole-H signal of $Fe(TPP)(THF)_2^+$ is 3.1 ppm, the contribution of the high-spin state in $[Fe(TPP)(THF)_2]^+$ is still not small.

Table 6
^{1}H NMR, ^{13}C NMR, and EPR data of $[Fe(TPP)L_2]^+$

Ligands (L)	^{1}H NMR[a]				^{13}C NMR[b]			EPR[c]		
	Py-H	*o*	*m*	*p*	α	β	*meso*	*g*-Values		
4-MePyNO	70.7	12.7	9.4	9.7	1625	1248	26	6.11	5.82	2.00
3,5-Me_2PyNO	71.0	12.8	9.4	9.7	1636	1249	29	5.85		2.00
PyNO	68.9	13.3	9.5	9.8	1617	1240	27	6.00		2.00
4-ClPyNO	67.2	13.2	9.7	9.9	1594	1218	25	5.85		2.00
DMSO	67.2	13.0	9.6	9.7	1538	1226	10	5.85		2.01
DMF	60.2	13.5	9.9	9.9	1474	1179	13	5.85		2.00
CH_3OH	48.1	13.8	10.1	10.0	1261	1024	37	5.69		2.00
THF	3.1	14.1	10.1	10.3	547	518	60	4.59	5.48	2.00
								6.03	5.48	2.00

Adapted from Refs. [92,93].
[a] CD_2Cl_2, 298 K.
[b] CD_2Cl_2, 298 K.
[c] CH_2Cl_2, 4.2 K.

Table 7
^{1}H NMR and EPR data of [Fe(TEtPrP)X] and [Fe(T^{i}PrP)X]

Complexes X	^{1}H NMR (CD_2Cl_2, 298 K)		Int[a] (%)	EPR (CD_2Cl_2, 4.2 K)			Int[b] (%)
	Py-H	CH_α		g-Values			
[Fe(TEtrPr)X]							
F	97.0	15.8	0	5.92	5.92	1.99	4
Cl	93.1	20.5	3	6.11	5.90	2.00	0
Br	85.2	22.2	9	5.95	5.93	1.99	3
I	60.4	22.7	28	5.50	3.02	1.80	87
I[c]	85.1	23.5	9	5.94	5.94	2.01	3
ClO_4	−33.9	10.2	100	4.09	4.09	1.98	97
[Fe(T^{i}PrP)X]							
F	97.1	22.3	0	5.95	5.95	2.00	3
Cl	90.4	28.3	5	6.16	5.71	2.00	3
Br	73.9	28.8	18	5.92	5.92	1.99	4
I	20.7	22.8	60	5.34	3.02	1.85	91
ClO_4	−31.2	13.8	100	4.90	3.50	1.90	90

Adapted from Ref. [97].
[a] Determined on the basis of the pyrrole-H chemical shifts at 298 K.
[b] Determined on the basis of the EPR g values at 4.2 K.
[c] In toluene-d_8 solution.

3.2. Effect of ruffled porphyrin ring on the spin state

3.2.1. Five-coordinate complexes

Ruffling of the porphyrin ring affects the energy levels of the iron d orbitals. As mentioned in the previous section, the d_{xy} orbital is destabilized by the interaction with the porphyrin (a_{2u}) orbital. In addition, the $d_{x^2-y^2}$ orbital is also destabilized due to the contraction of the equatorial Fe–N bonds, which is commonly observed in highly ruffled iron(III) porphyrin complexes [32,38,39,54]. Because of the destabilization of the $d_{x^2-y^2}$ orbital, the ruffled complexes tend to stabilize the intermediate-spin state. Table 7 a pure high-spin state. By contrast, the pyrrole signals of the ClO_4^- complexes appear at the most upfield positions, −34 and −31 ppm, and move further upfield almost linearly against $1/T$. Thus, the ClO_4^- complexes are considered to be in an essentially pure intermediate-spin state. The pyrrole signals of the Br^- and I^- complexes appear between those of the corresponding F^- and ClO_4^- complexes, suggesting that they are in the mixed spin state of the $S = 3/2$ and $S = 5/2$ with a sizable contribution of the $S = 5/2$. shows the ^{1}H NMR and EPR data of a series of five-coordinate [Fe(TEtPrP)X] and [Fe(T^{i}PrP)X] [97]. Fig. 15 shows the Curie plots of the pyrrole signals of these complexes [97]. The Curie lines are drawn so that they intercept the axis of ordinate at the chemical shifts of the corresponding diamagnetic complexes, ca. 9.5 ppm. In both [Fe(TEtPrP)X] and [Fe(T^{i}PrP)X], the pyrrole signals of the F^- complexes appear in the most downfield position, δ = ca. 97 ppm at 298 K, and move further downfield linearly against $1/T$. The pyrrole signals of the Cl^- complexes show similar temperature dependence. These results suggest that the F^- and Cl^- complexes in both systems are in Thus, in the ruffled complexes, even the iodide complexes exhibit a considerable contribution

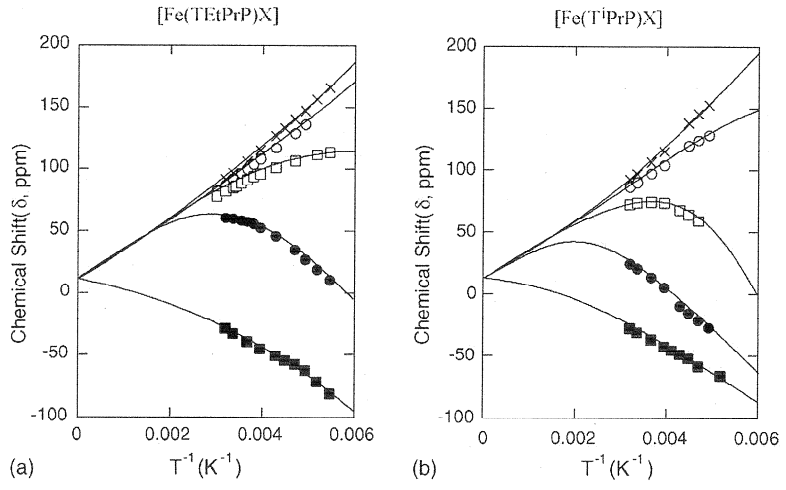

Fig. 15. Curie plots of the pyrrole-H signals of (a) Fe(TEtPrP)X and (b) Fe(T^{i}PrP)X taken in CD_2Cl_2 solution where X = F (×), Cl (○), Br (□), I (●), and ClO_4 (■). Adapted from Ref. [97].

of the $S = 3/2$. If we assume that the F^- and the ClO_4^- complexes are in a pure $S = 5/2$ and $S = 3/2$ spin state, respectively, then the contribution of the $S = 3/2$, which is signified as Int(%), can be estimated on the basis of the pyrrole-H chemical shifts by Eq. (6), where δ_F, δ_{ClO_4}, and δ_X are the pyrrole-H chemical shifts of the F^-, ClO_4^-, and X^- complexes, respectively [97]:

$$\text{Int}(\%) = \frac{\delta_F - \delta_X}{\delta_F - \delta_{ClO_4}} \times 100 \quad (6)$$

The data in Table 7 also indicate that the Int(%) value of five-coordinate [Fe(TEtPrP)I] is very much dependent on the solvent used. While the Int(%) is 28% at 298 K in CD_2Cl_2 solution, it is only 9% in toluene-d_8 solution at the same temperature.

The EPR g values of [Fe(TEtPrP)X] and [Fe(T^{i}PrP)X] are also listed in Table 7. Once the EPR g values are determined, it is possible to estimate the Int(%) values by Eq. (7) [74]:

$$\text{Int}(\%) = \frac{6.0 - g_\perp}{2} \times 100 \quad (7)$$

Thus, the complexes are in a pure high-spin state if $g_\perp$ is 6.0, while they are in a pure intermediate-spin state if $g_\perp$ is 4.0. The data in Table 7 suggest that, while the F^-, Cl^-, and Br^- complexes are essentially in the high spin state, the I^- complexes such as [Fe(TEtPrP)I] and [Fe(T^{i}PrP)I] are mainly in the intermediate-spin state with the Int(%) of 87 and 91%, respectively. Since the Int(%) values of [Fe(TEtPrP)I] and [Fe(T^{i}PrP)I] are estimated by the ^{1}H NMR method to be 28 and 60% at 298 K, respectively, they increase as the temperature is lowered from 298 to 4.2 K. In contrast, the Int(%) values of the Br^- complexes decrease with decreasing the temperature. The data in Table 7 also indicate that the Int(%) of [Fe(TEtPrP)I] varies depending on the conditions. Although the complex exhibits a mixed spin state in CH_2Cl_2 solution, it shows a quite pure high-spin state both in toluene solution and in the solid; the $g_\perp$ and $g_{||}$ values are 5.94 and 2.01 in toluene solution and 5.98 and 2.05 (not shown in Table 7) in the solid, respectively. The difference in spin states of [Fe(TEtPrP)I] in solution and in the solid is not a very unusual phenomenon. For example, iodo(etiohemiporphycenato)iron(III) exhibits the $S = 3/2$ with minor contribution of the $S = 5/2$ in solution [98]. The same complex shows, however, a quite pure $S = 5/2$ state in the solid. The difference is ascribed to the extraordinarily labile nature of the iodide ion in iodo(etiohemiporphycenato)iron(III). Thus, the iron is dragged toward the N4 cavity in solution and, consequently, the complex adopts the intermediate-spin state. In the crystal lattice, however, the packing force could contract the labile Fe–I bond. Thus, the iron is lifted from the N4 cavity toward the iodide, resulting in the formation of a typical high-spin five-coordinate structure. The difference in spin states of [Fe(TEtPrP)I] in solution and in the solid could be explained similarly. The labile nature of the spin state mentioned above is one of the characteristic features of the five-coordinate iron(III) porphyrin complexes, because similar ambiguity in the spin state has been observed in the five-coordinated iron(III) porphyrin complexes in the biological system such as cytochromes c' [99–101].

3.2.2. Six-coordinate complexes

The ^{1}H and ^{13}C NMR chemical shifts as well as EPR g values of a series of six-coordinate [Fe(T^{i}PrP)L_2]$^+$ are listed in Table 8 [92,93]. The axial ligands are arranged according to the magnetochemical series for oxygen ligands shown in Eq. (5). Comparison of the ^{1}H NMR chemical shifts between [Fe(TPP)L_2]$^+$ and [Fe(T^{i}PrP)L_2]$^+$ listed in Tables 6 and 8, respectively, reveals that each pyrrole-H signal shifts upfield to a different extent on going from planar [Fe(TPP)L_2]$^+$ to ruffled [Fe(T^{i}PrP)L_2]$^+$. Consequently, the difference in pyrrole-H chemical shifts increases among the 4-MePyNO, PyNO, 4-ClPyNO, and DMSO complexes, which enables us to rank the field strength for oxygen ligands as shown in Eq. (5). The ^{13}C NMR chemical shifts of the α and β signals correlate well with those of the pyrrole-H chemical shifts, suggesting that these signals can also be good probes to determine the contribution of the $S = 3/2$ spin state. In contras, the chemical shifts of the *meso* carbon signals exhibit a poor correlation. Combination of highly ruffled porphyrin ring and a fairly weak oxygen ligand leads to the formation of an essentially pure intermediate-spin complex. Typical examples are [Fe(TMCP)(EtOH)$_2$]$^+$ and [Fe(T^{i}PrP)(THF)$_2$]$^+$ [102–104].

Table 8
^{1}H NMR, ^{13}C NMR, and EPR data of [Fe(T^{i}PrP)L_2]$^+$

Ligands (L)	^{1}H NMR[a]			^{13}C NMR[b]			EPR[c]	
	Py-H	CH	CH_3	α	β	*meso*	*g*-Values	
4-MePyNO	58.5	10.8	6.2	1262	1038	97	5.85	2.00
3,5-Me_2PyNO	57.6	10.9	6.3	1239	1015	97	5.70	2.00
PyNO	41.7	9.9	6.1	1031	865	110	5.70	2.00
4-ClPyNO	35.2	10.7	5.8	889	756	114	5.75	1.99
DMSO	−7.7	8.0	4.6	226	290	126	4.2	2.00
DMF	−21.5	7.3	4.2	24	138	145	4.2, 4.1	2.00, 2 00
CH_3OH	−28.3	7.3	n.d.	−47	86	142	4.0	1.97
THF	−35.5	5.7	4.9	−122	22	115	4.1	2.00
Dioxane	−39.8	5.9	n.d.	−156	9	118	4.1	2.00

Adapted from Ref. [93].
[a] CD_2Cl_2, 298 K.
[b] CD_2Cl_2, 298 K.
[c] CH_2Cl_2, 4.2 K.

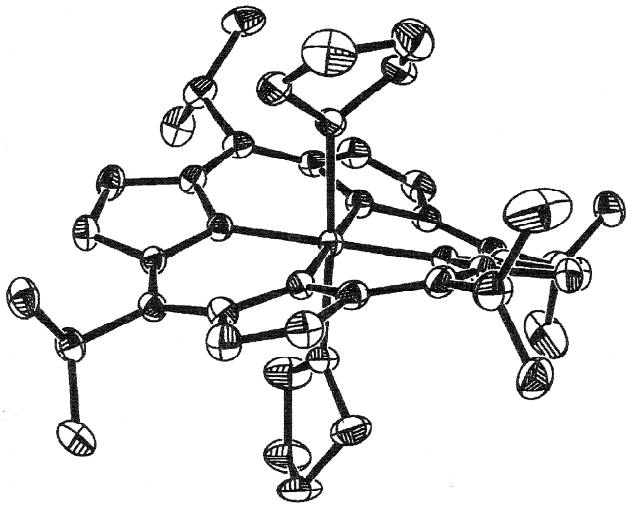

Fig. 16. ORTEP diagram of $[Fe(T^iPrP)(THF)_2]ClO_4$. Adapted from Ref. [105].

In Fig. 16 is given the molecular structure of $[Fe(T^iPrP)(THF)_2]^+$ [105]. The average equatorial Fe–N bond is very short, 1.967 Å, due to the highly ruffled structure, which should be compared with 1.999 and 2.040 Å in analogous $[Fe(OEP)(THF)_2]^+$ and $[Fe(TPP)(THF)_2]^+$ [106,107]. The average deviation of the *meso* carbon atoms from the mean porphyrin plane is 0.629 Å, which is smaller than the corresponding value, 0.72 Å, in low-spin $[Fe(TEtP)(2\text{-}MeIm)_2]^+$ shown in Fig. 7 [54].

3.3. Effect of saddled porphyrin ring on the spin state

3.3.1. Five-coordinate complexes

Saddling of the porphyrin core also affects the d orbital energy levels. Although the saddled deformation decreases the overlap between the iron $d_{x^2-y^2}$ and nitrogen lone pair because of the geometrical reason, it should enhance the interaction between the $d_{x^2-y^2}$ and the porphyrin a_{2u} orbital [15,108,109]; the latter interaction is possible in the saddled complexes as shown in Table 1. In addition, the interaction should be strengthened because the Fe–N bonds in OETPP complexes are in general much shorter than those of the corresponding TPP complexes. The most explicit example showing the $d_{x^2-y^2}$–a_{2u} interaction is radical cationic $[Cu(II)(OETPP)]^{\bullet+}$ reported by Fajer et al. [110]. The complex exhibits sharp ^1H NMR lines, indicative of diamagnetic species ascribed to the strong antiferromagnetic coupling between the unpaired electron in the $d_{x^2-y^2}$ orbital and the π radical in the a_{2u} orbital. Thus, the $d_{x^2-y^2}$ orbital can be destabilized in highly saddled complexes to increase the contribution of the intermediate-spin state. Table 9 shows the ^1H NMR and EPR data of a series of five-coordinate [Fe(OETPP)X], where $X = F^-$, Cl^-, Br^-, I^-, and ClO_4^- [111,112]. The Int(%) values estimated at 4.2 K by Eq. (7) clearly indicates that, while the F^- and Cl^- complexes are in the $S = 5/2$ with a minor contribution of the $S = 3/2$, the Br^- and I^- complexes adopt the $S = 3/2$ with a minor contribution of the $S = 5/2$. In the case of the ClO_4 complex, it exhibits an essentially pure $S = 3/2$ spin state. The Int(%) values of ruffled [Fe(TEtPrP)Br] and saddlcd [Fe(OETPP)Br] are 4 and 89%, respectively, at 4.2 K. Thus, the saddled OETPP core stabilizes the $S = 3/2$ state more effectively than the corresponding ruffled T^iPrP core for the same axial ligand. The possibility that the saddled porphyrin ring would stabilize the intermediate-spin state was first proposed by Cheng et al. in a discussion of the spin state of [Fe(OETPP)Cl] [113]. Although the Int(%) of [Fe(OETPP)Cl] is not so high as proposed [114], the saddled complexes such as $[Fe(OETPP)]ClO_4$ and [Fe(OETPP)I] are certainly in a quite pure intermediate spin state [111,112].

3.3.2. Six-coordinate complexes

The ^1H NMR, ^{13}C NMR, and EPR data of a series of six-coordinate $[Fe(OETPP)L_2]^+$ are listed in Table 10 [93]. The complexes with weak axial ligands such as THF, MeOH, DMF, and DMSO exhibit the $g_\perp$ signals at 4.0–4.2, suggesting that the complexes are in an essentially pure intermediate-spin state. These complexes commonly exhibit the *meso* signals fairly upfield, which should be ascribed to the interaction between the filled a_{2u} and empty $d_{x^2-y^2}$ orbital in saddle shaped complexes [15]. This interaction induces the negative spin to the a_{2u} orbital by the spin polarization mechanism and shifts the *meso* carbon signal to the upfield position [15]. In addition, the $d_\pi - 3e_g$ interaction should also contribute to the upfield shift of the *meso* carbon signals as shown in Eq. (1), especially when the complexes adopt the $(d_{xy})^2(d_{xz}, d_{yz})^2(d_{z^2})^1$ electron configuration because of the presence of two unpaired electrons in the d_π orbitals [93,104]. The electron configuration of the saddle shaped complexes showing the $S = 3/2$ spin state such as $[Fe(OETPP)(THF)_2]^+$ is, however, quite controversial. Nakamura et al. reported that the complex adopts the $(d_{xy})^2(d_{xz}, d_{yz})^2(d_{z^2})^1$ electron configuration on the basis of the ^1H NMR,

Table 9
^1H NMR and EPR Data of Fe(OETPP)X

Complexes	^1H NMR (CD_2Cl_2, 298 K)						EPR (CH_2Cl_2, 4.2 K)			Int[a] (%)
	CH_2		CH_3	*o*	*m*	*p*	*g*-Values			
Fe(OETPP)F	24.1, 38.4	35.4, 45.0	1.6, 3.7	8.1, 10.6	12.9, 13.1	7.0	6.50	5.30	2.00	5
Fe(OETPP)Cl	20.1, 34.8	32.1, 49.0	1.8, 3.2	9.1, 11.5	12.2, 12.4	7.5	6.56	5.27	1.97	4
Fe(OETPP)Br	18.1, 34.3	32.6, 45.8	1.0, 2.3	10.4, 13.5	11.7, 12.2	8.4	4.95	3.50	1.95	89
Fe(OETPP)I	11.9, 32.1	29.3, 47.3	0.4, 0.9	12.6, 15.8	10.3, 10.8	9.6	4.14	4.14	2.00	93
Fe(OETPP)ClO_4	13.0	42.7	0.7	13.4	7.1	9.8	4.05	4.05	2.1	98

Adapted from Refs. [111,112].
[a] Determined on the basis of the EPR *g* values at 4.2 K.

Table 10
^{1}H and ^{13}C NMR chemical shifts of $[Fe(OETPP)L_2]^+$

Ligand	^{1}H NMR[a]						^{13}C NMR[b]			EPR[c]		
	CH_2		CH_3	*o*	*m*	*p*	α	β	*meso*	*g*-Values		
4-MePyNO	21.0	44.2	2.4	14.7	8.7	10.3	598	601	−19	5.54		2.00
3,5-Me_2PyNO	18.6	43.8	2.4	14.7	8.4	10.4	504	498	−40	5.69		2.00
PyNO	20.0	43.8	2.2	15.3	7.4	10.6	555	512	−63	5.73	4.35	2.00
DMSO	15.4	39.2	0.9	17.2	7.4	10.6	485	398	−139	4.2		2.01
DMF	11.6	37.7	−0.1	15.8	6.1	11.4	419	250	−221	4.2		2.00
MeOH	11.7	37.0	0.3	15.8	5.9	11.5	409	239	−211	4.1		1.97
THF	11.1[d]	38.7	0.3	15.8[d]	5.6	11.5	394	215	−269[d]	4.0		2.00

Adapted from Ref. [93].
[a] CD_2Cl_2, 298 K.
[b] CD_2Cl_2, 298 K.
[c] CH_2Cl_2, 4.2 K.
[d] Values are revised from the original ones [118].

^{13}C NMR, and EPR data [93,104]. By contrast, Cheng et al. proposed on the basis of the DFT calculation that the complex should adopt the $(d_{xz}, d_{yz})^3(d_{xy})^1(d_{z^2})^1$ electron configuration since the d_{xy} orbital of iron is destabilized due to the d_{xy}–a_{1u} interaction to the point that is higher than the d_π orbitals; the d_{xy}–a_{1u} interaction is possible in saddle shaped complex as shown in Table 1 [15]. Obviously, more experimental and theoretical studies are necessary to describe the real electronic nature of saddle shaped intermediate-spin complexes.

4. Spin-crossover in saddled complexes

4.1. General consideration

In iron(III) porphyrinates, the five d orbitals can be formally arranged into three possible spin states. They are the high-spin $S = 5/2$, the low-spin $S = 1/2$, and the intermediate-spin $S = 3/2$ state. Some complexes exhibit the spin crossover phenomenon between two states caused by the temperature, pressure, photoirradiation, etc. as shown in Fig. 17. The spin crossover between the $S = 5/2$ and $S = 1/2$ has been most extensively studied in six-coordinated complexes such as $[Fe(OEP)(3\text{-}ClPy)_2]^+$, $[Fe(TPP)(N_3)_2]$, and $[Fe(OEP)(N_3)(1\text{-}MeIm)]$ [115–118]. On the other hand, the spin crossover between the $S = 5/2$ and $S = 3/2$ has never been observed, because the mixed $S = 5/2$, 3/2 spin state is considered to be a quantum mechanical spin admixture caused by the spin–orbit coupling between the $S = 5/2$ and $S = 3/2$ spin states [83], and not a thermal equilibrium between the $S = 3/2$ and $S = 5/2$ spin states. In fact, no clear example has ever been reported showing that the complex exists as a mixture of the $S = 3/2$ and $S = 5/2$. The spin crossover between the $S = 3/2$ and $S = 1/2$ is quite rare because of the instability of the intermediate-spin complex. Quite recently, it was found that saddle shaped $[Fe(OETPP)Py_2]^+$ exhibits such a phenomenon both in solution and in the solid [119]. Understanding this phenomenon is quite important since recent studies have revealed that the similar spin crossover process could be taking place in ferric heme in heme oxygenase [60,61,82]. In this chapter, a novel spin crossover process between the $S = 3/2$ and $S = 1/2$ in saddle shaped $[Fe(OETPP)L_2]^+$ and $[Fe(OMTPP)L_2]^+$ is considered.

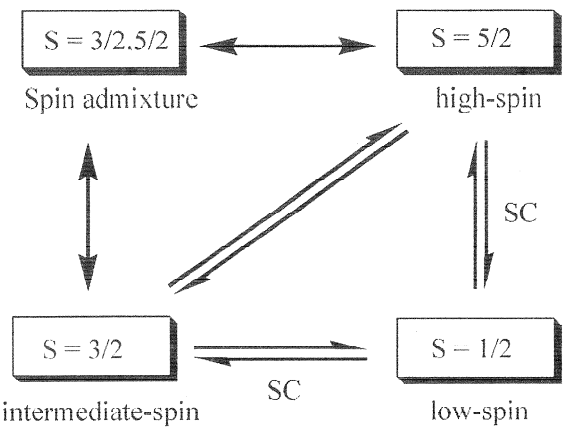

Fig. 17. Spin crossover (SC) between two states.

4.2. Magnetic behavior in solution

4.2.1. $[Fe(OETPP)L_2]^+$

Six-coordinate complexes with nitrogen base such as imidazole or pyridine usually show the low-spin state [40]. As mentioned in the previous chapter, the saddle shaped complexes tend to stabilize the intermediate-spin state. Typical examples are [Fe(OETPP)I] and $[Fe(OETPP)(THF)_2]^+$ [103,111]. The Int(%) values of these complexes are determined to be 93 and 100% at 4.2 K, respectively. It is then expected that even the complexes carrying nitrogen bases with weak field strength should exhibit a quite pure $S = 3/2$ spin state if the porphyrin is highly saddled; $[Fe(OEP)(3,5\text{-}Cl_2Py)_2]^+$ is known to show a mixed spin state [120]. Table 11 lists the ^{1}H and ^{13}C NMR chemical shifts of $[Fe(OETPP)L_2]^+$ and $[Fe(OMTPP)L_2]^+$ where L's are nitrogen bases [93,121]. The chemical shifts of $[Fe(OETPP)(^tBuNC)_2]^+$, which is well characterized as the $S = 1/2$ complex adopting the $(d_{xz}, d_{yz})^4(d_{xy})^1$ ground state, are also listed for comparison [47,103]. As the axial ligand changes from HIm to 4-CNPy in Table 11, the CH_α, *o*-H, and *p*-H signals of $[Fe(OETPP)L_2]^+$ exhibit a large downfield shift and approach to the corresponding

Table 11
^{1}H NMR chemical shifts of $[Fe(OETPP)L_2]^+$ and $[Fe(OMTPP)L_2]^+$ taken in CD_2Cl_2 solution at 298 K

Complexes L	^{1}H NMR					^{13}C NMR		
	CH_α		*o*-H	*m*-H	*p*-H	*meso*	α	β
$[Fe(OETPP)L_2]^+$								
HIm	4.4	10.3	5.8	5.8	6.7	7	163	167
DMAP	4.8	11.8	5.4	5.9	6.9	3	168	176
Py	11.1	32.3	13.0	5.8	10.4	−186	384	244
4-CNPy	13.7[a]	41.8	16.5[a]	5.3	12.1	−295[a]	470	266
^{t}BuNC	7.5		5.5	11.1	6.3	419	−4	144
$[Fe(OMTPP)L_2]^+$								
HIm	19.8		5.4	6.2	6.8	30	128	173
DMAP	19.7		5.3	6.4	6.7	48	110	164
Py	48.6		10.8	7.2	9.1	−9	205	214
4-CNPy	63.9		13.2	6.8	10.2	−68	243	242
^{t}BuNC	1.4		3.1	12.8	5.2	701	−207	113

Adapted from Ref. [121].
[a] Values are revised from the original ones.

signals of $[Fe(OETPP)(THF)_2]^+$ listed in Table 10. In addition, the large upfield shift of the *meso* and the downfield shift of the α carbon signals of $[Fe(OETPP)(4\text{-}CNPy)_2]^+$ resemble those of $[Fe(OETPP)(THF)_2]^+$. These NMR results suggest that the spin state actually changes from the $S = 1/2$ in the HIm and DMAP complexes to the $S = 3/2$ in the 4-CNPy complex. In fact, the solution magnetic moment of $[Fe(OETPP)(4\text{-}CNPy)_2]^+$ determined by the Evans method [122] in CD_2Cl_2 solution is $4.2 \pm 0.1\ \mu_B$ at 193–298 K, which is close to the spin only value expected for the $S = 3/2$ complexes. It is interesting to compare the electronic structures of saddled $[Fe(OETPP)L_2]^+$ carrying nitrogen bases with those of corresponding ruffled $[Fe(T^iPrP)L_2]^+$. In the case of ruffled $[Fe(T^iPrP)L_2]^+$, all the complexes maintain the low-spin state although the electron configuration changes from $(d_{xy})^2(d_{xz}, d_{yz})^3$ to $(d_{xz}, d_{yz})^4(d_{xy})^1$ as the field-strengths of the axial ligands are weakened; axial ligands with strong σ donating ability such as HIm and DMAP stabilize the $(d_{xy})^2(d_{xz}, d_{yz})^3$ ground state while those with weak σ donating and strong π accepting ligands such as 4-CNPy stabilize the $(d_{xz}, d_{yz})^4(d_{xy})^1$ ground state [43]. In the case of saddled $Fe(OETPP)L_2^+$, however, it is the spin state that changes depending on the field strength of the axial ligands. While the strong σ donating ligands give the low-spin complex with the $(d_{xy})^2(d_{xz}, d_{yz})^3$ ground state, the weak σ donating and strong π-accepting ligands form the intermediate-spin complexes. Fig. 18 summarizes the difference in electronic structures between ruffled $[Fe(T^iPrP)L_2]^+$ and saddled $[Fe(OETPP)L_2]^+$ carrying axially coordinating nitrogen bases.

The data in Table 11 indicate that the ^{1}H and ^{13}C signals of $[Fe(OETPP)Py_2]^+$ are located between those of low-spin $[Fe(OETPP)(DMAP)_2]^+$ and intermediate-spin $[Fe(OETPP)(4\text{-}CNPy)_2]^+$, suggesting that both the low-spin and intermediate-spin $[Fe(OETPP)Py_2]^+$ coexist as an equilibrium mixture in CD_2Cl_2 solution at 298 K [119]. Fig. 19(a) shows the Curie plots of the CH_2 signals of $[Fe(OETPP)L_2]^+$, where L's are DMAP, Py, and 4-CNPy. While the Curie lines of the DMAP and 4-CNPy complexes are linear, the Curie line of the Py complex exhibits a considerable curvature. Similar tendency is observed in the Curie plots of the *meso* carbon signals shown in Fig. 19(b). Although both the CH_2 and *meso*-^{13}C signals of the Py complex appear close to the corresponding signals of the 4-CNPy complex at ambient temperature, they approach to those of the DMAP complex at lower temperature. The curvature of the Curie lines of $[Fe(OETPP)Py_2]^+$ clearly indicate that the spin crossover takes place between the $S = 3/2$ and $S = 1/2$. In contrast, $[Fe(OETPP)(DMAP)_2]^+$ and $[Fe(OETPP)(4\text{-}CNPy)_2]^+$ maintain the $S = 1/2$ and $S = 3/2$ spin state, respectively, in the temperature range examined. The equilibrium constant (K_{SC}) for the spin crossover process in CD_2Cl_2 solution is determined at several temperatures on the basis of the chemical shifts according to Eq. (8), where δ_{DMAP}, δ_{Py}, and $\delta_{4\text{-}CNPy}$ are the *meso*-^{13}C chemical shifts of the DMAP, Py, and 4-CNPy complexes, respectively. The plots of $\log(K_{SC})$ versus $1/T$ shows:

$$K_{SC} = \frac{[S = 3/2]}{[S = 1/2]} = \frac{[\delta_{DMAP} - \delta_{Py}]}{[\delta_{Py} - \delta_{4\text{-}CNPy}]} \quad (8)$$

a good linearity from which the thermodynamic parameters are determined as follows: $\Delta H^\circ = 17\ kJ\ mol^{-1}$ and

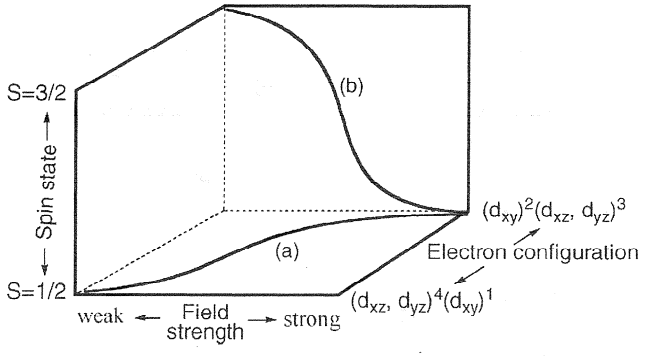

Fig. 18. Schematic diagram on the change in electronic structures of (a) ruffled $[Fe(T^iPrP)L_2]^+$ and (b) saddled $[Fe(OETPP)L_2]^+$ as the axial ligand changes from strong Him to weak 4-CNPy. While the electron configuration changes from $(d_{xy})^2(d_{xz}, d_{yz})^3$ to $(d_{xz}, d_{yz})^4(d_{xy})^1$ in the case of ruffled $[Fe(T^iPrP)L_2]^+$, the spin state changes from the $S = 1/2$ to the $S = 3/2$ in the case of saddled $[Fe(OETPP)L_2]^+$.

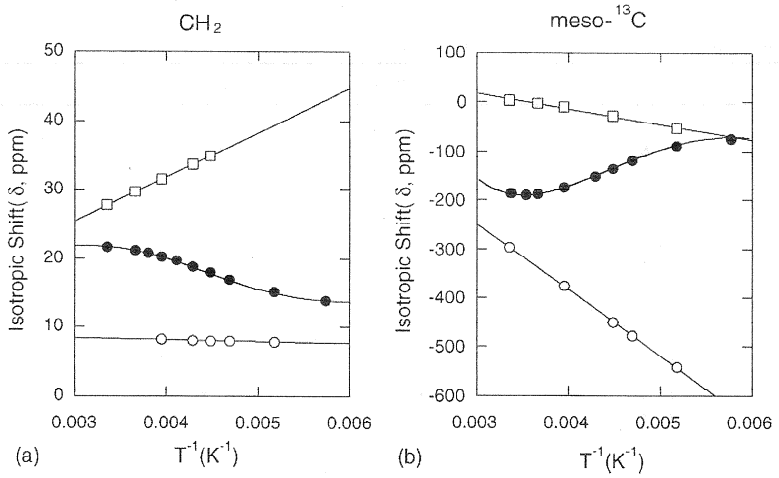

Fig. 19. Curie plots of the (a) CH_2 and (b) *meso*-^{13}C signals of $[Fe(OETPP)(DMAP)_2]^+$ (○), $[Fe(OETPP)(Py)_2]^+$ (●), and $[Fe(OETPP)(4\text{-}CNPy)_2]^+$ (□). Adapted from Ref. [119].

$\Delta S^\circ = 67\ J\ mol^{-1}\ K^{-1}$ [119]. Although the spin-crossover process between the $S = 1/2$ and $S = 3/2$ states is not unprecedented in Fe(III) complexes [123,124], $[Fe(OETPP)Py_2]^+$ is actually the first example in the porphyrin complexes. It should be noted that $[Fe(OETPP)Py_2]^+$ adopts the $(d_{xy})^2(d_{xz}, d_{yz})^3$ ground state at lower temperature on the basis of the ^1H and ^{13}C NMR chemical shifts [121].

4.2.2. *Fe(OMTPP)L$_2$$^+$*

Fig. 20 shows the Curie plots of the CH_3 and *meso*-^{13}C signals of $[Fe(OMTPP)L_2]^+$ where L's are DMAP, Py, 4-CNPy, THF, and ^{t}BuNC [121]. Among these complexes, $[Fe(OMTPP)(THF)_2]^+$ is in a quite pure intermediate-spin state while $[Fe(OMTPP)(DMAP)_2]^+$ and $[Fe(OMTPP)(^t BuNC)_2]^+$ adopt the low-spin state with the $(d_{xy})^2(d_{xz}, d_{yz})^3$ and $(d_{xz}, d_{yz})^4(d_{xy})^1$ electron configuration, respectively [47,121]. The Curie lines of $[Fe(OMTPP)Py_2]^+$ and $[Fe(OMTPP)(4\text{-}CNPy)_2]^+$ shown in Fig. 20(a) exhibit a curvature, suggesting that the spin crossover takes place in both of these complexes between $S = 3/2$ and $S = 1/2$. Inspection of the Curie lines for the *meso*-^{13}C signals shown in Fig. 20(b) reveals, however, that the magnetic behaviors of $[Fe(OMTPP)L_2]^+$ (L = Py and 4-CNPy) are quite different form those of $[Fe(OETPP)L_2]^+$ (L = Py). As the temperature is lowered, the Curie line of $[Fe(OMTPP)(4\text{-}CNPy)_2]^+$ moves away from that of $[Fe(OMTPP)(DMAP)_2]^+$, and rather approaches that of $[Fe(OMTPP)(^t BuNC)_2]^+$. Similar temperature dependence is observed for $[Fe(OMTPP)Py_2]^+$ though the deviation from the Curie line of $[Fe(OMTPP)(DMAP)_2]^+$ is much smaller. These results suggest that the spin crossover pathways are different between the OETPP and OMTPP complexes. In contrast to the case of the OETPP complex, the OMTPP complexes approach the $S = 1/2$ state with the $(d_{xz}, d_{yz})^4(d_{xy})^1$ ground state as the temperature is lowered [121,125].

4.3. Magnetic behavior in the solid

4.3.1. *Fe(OETPP)L$_2$$^+$*

Table 12 lists the Mössbauer parameters of a series of $[Fe(OETPP)L_2]^+$ measured at ambient and liquid nitrogen tem-

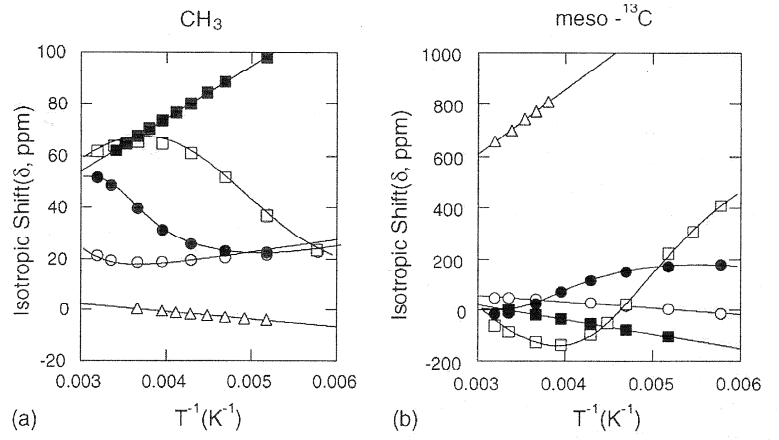

Fig. 20. Curie plots of the (a) CH_3 and (b) *meso*-^{13}C signals of $[Fe(OMTPP)(DMAP)_2]^+$ (○), $[Fe(OMTPP)(Py)_2]^+$ (●), $[Fe(OMTPP)(4\text{-}CNPy)_2]^+$ (□), $[Fe(OMTPP)(THF)_2]^+$ (■), and $[Fe(OMTPP)(^t BuNC)_2]^+$ (Δ). Adapted from Ref. [121].

Table 12
Mössbauer parameters and spin states of $[Fe(OETPP)L]_2^+$ and $[Fe(OMTPP)L_2]^+$

Complexes L	T (K)	IS (mm s^{-1})	QS (mm s^{-1})	Γ_1 (mm s^{-1})	Γ_2 (mm s^{-1})	S
$[Fe(OETPP)L_2]^+$						
DMAP	290	0.19	2.21	0.27	0.32	1/2
	80	0.26	2.31	0.55	0.89	1/2
Py	290	0.32	2.76	0.27	0.29	3/2, 1/2
	80	0.25	2.29	0.47	0.64	1/2
4-CNPy						
Site A	295	0.37	3.26	0.32	0.33	3/2
Site A	80	0.57	3.03	0.47	0.47	3/2
Site B	80	0.20	2.70	0.64	0.64	1/2
THF	290	0.41	3.65	0.32	0.26	3/2
	80	0.50	3.50	0.77	0.49	3/2
$[Fe(OMTPP)L_2]^+$						
DMAP	290	0.16	1.86	0.30	0.33	1/2
	70	0.23	1.89	0.38	0.54	1/2
Py	299	0.19	2.18	0.23	0.26	1/2
	78	0.25	2.18	0.33	0.42	1/2

Adapted from Refs. [77,119].

peratures [77,119]. At ambient temperature, the quadrupole splitting (QS) value of $Fe(OETPP)(DMAP)_2^+$ is 2.21 mm s^{-1}, which is within the range of low-spin state [126–128]. In contrast, the QS value of $[Fe(OETPP)(4\text{-}CNPy)_2]^+$ is quite large, 3.26 mm s^{-1} and is close to that of $[Fe(OETPP)(THF)_2]^+$, suggesting that the complex adopts the intermediate-spin state. The QS value of $[Fe(OETPP)Py_2]^+$ is 2.76 mm s^{-1}, which is just between the QS values of $[Fe(OETPP)(DMAP)_2]^+$ and $[Fe(OETPP)(4\text{-}CNPy)_2]^+$. Thus, the Py complex exists as the mixture of the $S = 3/2$ and the $S = 1/2$ spin states at ambient temperature in the solid. As the temperature is lowered to 80 K, the QS value of the DMAP complex is maintained while that of the Py complex decreases to 2.26 mm s^{-1}. The results indicate that the Py complex adopts predominantly the low-spin state at 80 K. In the case of the 4-CNPy complex, two doublets (Sites A and B) appear below 230 K. Since the IS and QS values for sites A and B are in the range of intermediate-spin and low-spin states, respectively, the complexes with the different spin states coexist at low temperature. This implies that a novel spin crossover occurs also in $[Fe(OETPP)(4\text{-}CNPy)_2]^+$ in the solid state.

Fig. 21 shows the effective magnetic moments (μ_{eff}) measured on microcrystalline samples with a SQUID magnetometer over 2–300 K [119]. The results confirm that the DMAP complex is in the low-spin state while the THF complex is in the quite pure intermediate-spin state over wide range of temperatures. Fig. 21 also indicates that a major part of the Py complex is in the $S = 1/2$ below 150 K though the population of the $S = 3/2$ considerably increases above this temperature. Similarly, the 4-CNPy complex is a mixture of the $S = 1/2$ and $S = 3/2$ below 200 K though it exists almost exclusively as the $S = 3/2$ above 200 K. On the basis of the Mössbauer and SQUID results, it is clear that not only $[Fe(OETPP)Py_2]^+$ but also $[Fe(OETPP)(4\text{-}CNPy)_2]^+$ exhibits the spin crossover process in the solid.

4.3.2. $Fe(OMTPP)L_2^+$

Table 12 also shows the Mössbauer parameters of $[Fe(OMTPP)(DMAP)_2]^+$ and $[Fe(OMTPP)Py_2]^+$ [77]. The IS values increase from 0.16 to 0.23 mm s^{-1} in $[Fe(OMTPP)(DMAP)_2]^+$ and from 0.19 to 0.25 mm s^{-1} in $[Fe(OMTPP)(Py)_2]^+$ as the temperature is lowered from 290 to 77 K. In contrast, the QS values are almost constant in this temperature range; they are 1.86–1.90 mm s^{-1}

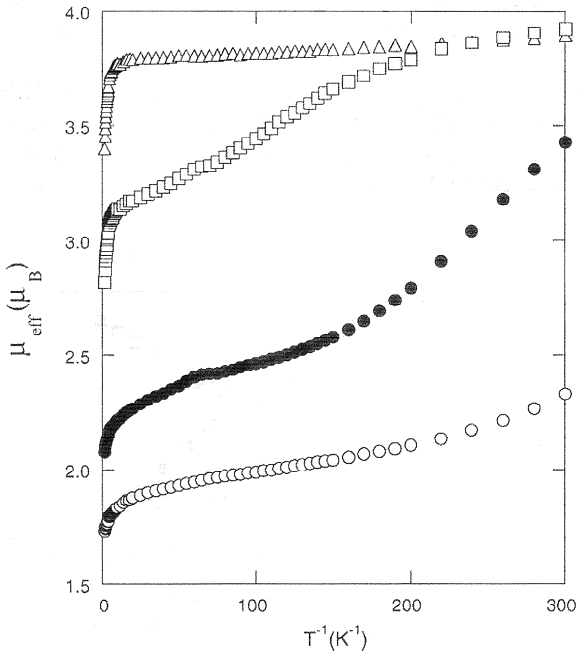

Fig. 21. Temperature dependence of the effective magnetic moments of $[Fe(OETPP)L_2]^+$. L = DMAP (○); Py (●); 4-CNPy (□); THF (Δ). Adapted from Ref. [119].

for $[Fe(OMTPP)(DMAP)_2]^+$ and 2.13–2.18 mm s^{-1} for $[Fe(OMTPP)Py_2]^+$. Thus, these complexes maintain the low-spin state over a wide range of temperature. The low spin state of $[Fe(OMTPP)(DMAP)_2]^+$ and $[Fe(OMTPP)Py_2]^+$ is further supported by the effective magnetic moments determined by SQUID magnetometry; they are 2.1–2.8 μ_B in the temperature range 50 to 300 K. Thus, the magnetic behaviors of $[Fe(OETPP)Py_2]^+$ and $[Fe(OMTPP)Py_2]^+$ are quite different in the solid. While $[Fe(OETPP)Py_2]^+$ shows a spin crossover between the $S = 3/2$ and $S = 1/2$, $[Fe(OMTPP)Py_2]^+$ maintains the $S = 1/2$ spin state [77].

4.3.3. Structural consequences of spin crossover

$[Fe(OETPP)Py_2]^+$ is a complex which shows a novel spin crossover both in solution and in the solid. It is quite interesting to know how the coordination structure and the surrounding lattice change during the spin transition process in the solid state. To solve this question, Ohgo et al. have examined the temperature dependence of the crystal and molecular structures of $[Fe(OETPP)Py_2]^+$ and $[Fe(OMTPP)Py_2]^+$ by the X-ray crystallographic analysis [77,129]. Fig. 22 shows molecular structures of $[Fe(OETPP)Py_2]^+$ and $[Fe(OMTPP)Py_2]^+$ determined at 298 K together with the perpendicular displacements of the peripheral atoms from the least-squares plane. The maximum deviation among the $C_{20}N_4Fe$ core is observed for one of the β carbon atoms, which is 1.31 Å for $[Fe(OETPP)Py_2]^+$ and 1.10 Å for $[Fe(OMTPP)Py_2]^+$. Deviation of the *meso* carbon from the least-squares plane is at most 0.05 Å in $[Fe(OETPP)Py_2]^+$ while it is as much as 0.19 Å in $[Fe(OMTPP)Py_2]^+$. Thus, the OETPP complex adopts a quite pure saddled structure while the OMTPP core includes some ruffling. This does not mean that the saddled OMTPP core is much easier to ruffle than the corresponding OETPP core. Structural analysis of $[Fe(OMTPP)(^tBuNC)_2]ClO_4$ reveals that the OMTPP core shows a quite pure saddled structure in spite of the coordination of ^{t}BuNC which usually induces the ruffled deformation of the porphyrin core [125].

Fig. 23 shows the crystal structure of $[Fe(OETPP)Py_2]ClO_4$ obtained at 298 K. As the temperature is lowered, the thermal motion of the molecules, especially that of the peripheral substituents, is restrained. The low temperature also decreases the thermal motion of each bond, inducing the bond contraction. As a result, the void space around the molecules increases, which requires the realignment of each molecule to achieve better crystallinity for the contracted molecules. Table 13 lists the crystal and structural data of $[Fe(OETPP)Py_2]^+$ together with those of $[Fe(OMTPP)Py_2]^+$. The data in Table 13 indicate that the unit cell decreases by 9.3% in volume on going from 298 to 80 K because of the packing force. It should be noted that the *a*-, *c*-, and *b*-axes almost coincide with the N1–N3, N2–N4, and N5–N6 axes, respectively; N1–N4 are porphyrin nitrogen atoms while N5 and N6 are pyridine nitrogen atoms. Close examination of the crystal data in Table 13 reveals that the lattice contraction along the *a*-, *c*-, and *b*-axes are 0.8, 2.1, and 8.8%, respectively, in the temperature range 298–80 K. Correspondingly, the bond contraction takes place by 1.4 and 9.4% for the Fe–N_p and Fe–N_{axial}, respectively. The largest contraction of the unit cell

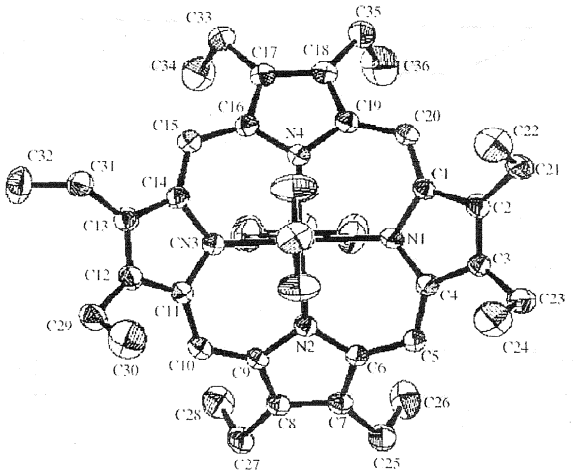

(a) $[Fe(OETPP)Py_2]ClO_4$

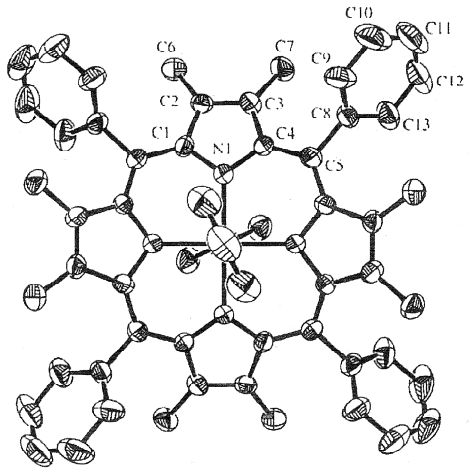

(b) $[Fe(OMTPP)Py_2]ClO_4$

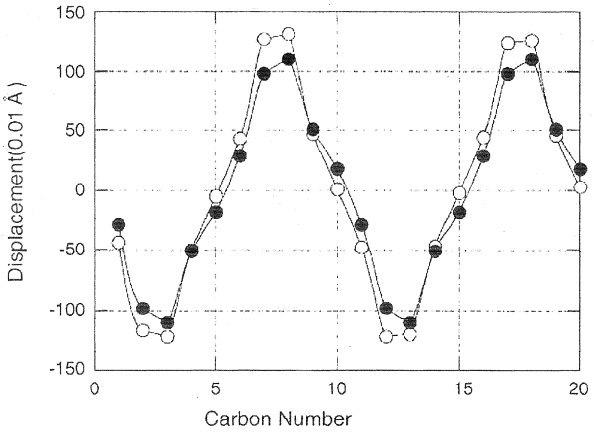

(c) Perpendicular displacement

Fig. 22. ORTEP diagrams of (a) $[Fe(OETPP)Py_2]^+$ and (b) $[Fe(OMTPP)Py_2]^+$. (c) Perpendicular displacement of the core atoms from the mean plane for $[Fe(OETPP)Py_2]^+$ and $[Fe(OMTPP)Py_2]^+$. Adapted from Refs. [77,129].

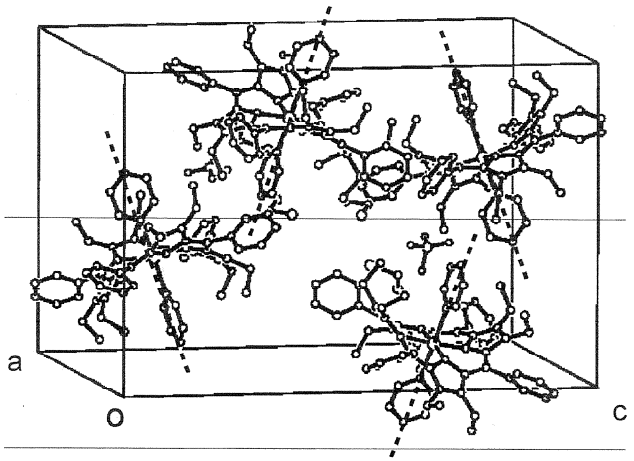

Fig. 23. The crystal structure of $[Fe(OETPP)Py_2]ClO_4$ obtained at 298 K. The dotted lines show the N(5)–Fe–N(6) axes. Adapted from Ref. [129].

occurs along the *b*-axis, which induces the largest contraction to the Fe–N_{axial} bonds. It is this shortening of the axial bonds at lower temperature that destabilizes the d_{z^2} orbital and induces the spin transition from the $S = 3/2$ to the $S = 1/2$ [129].

Table 13
Crystal and structural data for $[Fe(OETPP)Py_2]ClO_4$ and $[Fe(OMTPP)Py_2]ClO_4$[a]

	298 (K)	80 (K)
$[Fe(OETPP)Py_2]ClO_4$		
Crystal system	Monoclinic	Monoclinic
Space group	$P2_1/n$	$P2_1/n$
Z	4	4
a (Å)	13.972(1)	13.857(1)
b (Å)	19.481(1)	17.764(1)
c (Å)	26.750(3)	26.184(2)
β (°)	101.493(3)	101.411(1)
V (Å^3)	6969.0(10)	6318.0(6)
ave Fe–N_p (Å)	1.985(3)	1.957(3)
ave Fe–N_{axial} (Å)	2.201(3)	1.993(3)
ϕ (°)	1.1, 3.6	6.3, 11.6
θ (°)	82.3	85.1
Cavity (Å^3)	28.88, 32.08	23.19
$[Fe(OMTPP)Py_2]ClO_4$		
Crystal system	Cubic	Cubic
Space group	*I*43*d* (#220)	*I*43*d* (#220)
Z	12	12
a (Å)	25.937(1)	25.609(1)
b (Å)	25.937(1)	25.609(1)
c (Å)	25.937(3)	25.609(2)
α (°)	90	90
β (°)	90	90
γ (°)	90	90
V (Å^3)	17448(3)	16795.5(9)
ave Fe–N_p (Å)	1.963(3)	1.973(3)
ave Fe–N_{axial} (Å)	2.058(6)	2.024(4)
ϕ (°)	24.8	23.4
θ (°)	90	90
Cavity (Å^3)	19.81	18.77

Adapted from Ref. [77].
[a] Values in parenthesis are the % ratios relative to the values at 298 K.

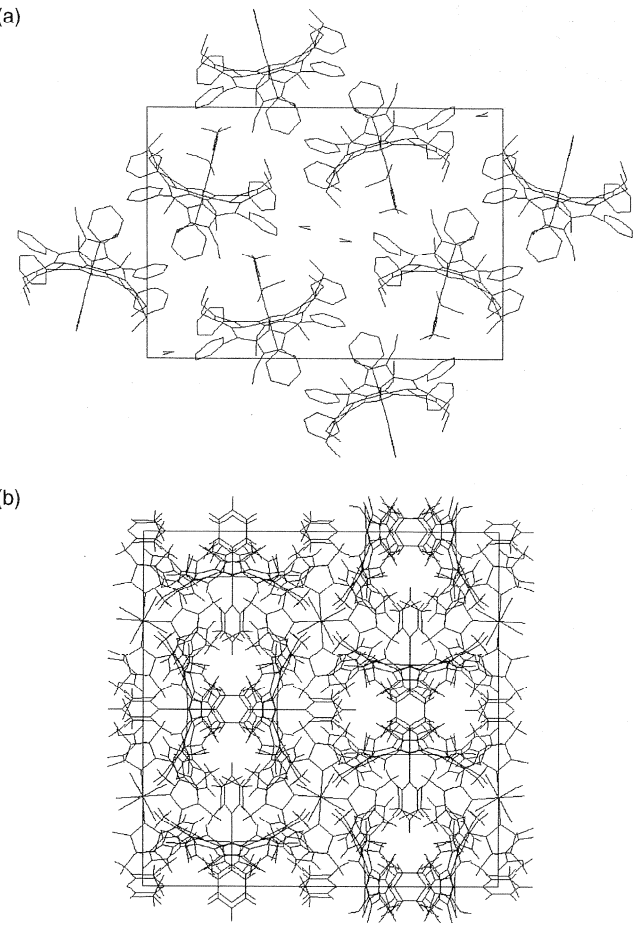

Fig. 24. Crystal packing diagrams of (a) monoclinic $[Fe(OETPP)Py_2]^+$ and (b)cubic $[Fe(OMTPP)Py_2]^+$ viewing along the *a*-axis. Adapted from Ref. [77].

4.3.4. *Importance of crystal packing*

The absence of the spin crossover process in $[Fe(OMTPP)Py_2]^+$ in the solid is ascribed to the crystal and molecular structures of this complex. The structural parameters listed in Table 13 indicate that the temperature dependent structural changes are fairly small in all respects including bond lengths and dihedral angles. For example, the Fe–N_{axial} bond in $[Fe(OMTPP)Py_2]^+$ shows only a slight decrease, 0.034 Å, as the temperature is lowered from 298 to 80 K in contrast to the case of $[Fe(OETPP)Py_2]^+$ where the decrease reaches as much as 0.208 Å. Similarly, rotation of the pyridine ligands is only 1.4° in $[Fe(OMTPP)Py_2]^+$ as compared with 6.6° (ave) in $[Fe(OETPP)Py_2]^+$. Fig. 24 shows the crystal packing diagrams of $[Fe(OETPP)Py_2]^+$ and $[Fe(OMTPP)Py_2]^+$; the former adopts a monoclinic while the latter shows a cubic crystal system. The monoclinic system is a less condensed packing form than cubic system [77]. In fact, the density of $[Fe(OMTPP)Py_2]^+$ with cubic crystal system is 1.406 g cm^{-3}, while that of monoclinic $[Fe(OETPP)Py_2]^+$ is only 1.296 g cm^{-3} at 298 K. In other words, the Fe–N_{axial} bond contraction in $[Fe(OMTPP)Py_2]^+$ at lower temperature is more difficult than that in $[Fe(OETPP)Py_2]^+$ since each molecule of $[Fe(OMTPP)Py_2]^+$ is placed in a densely packed crystal lattice

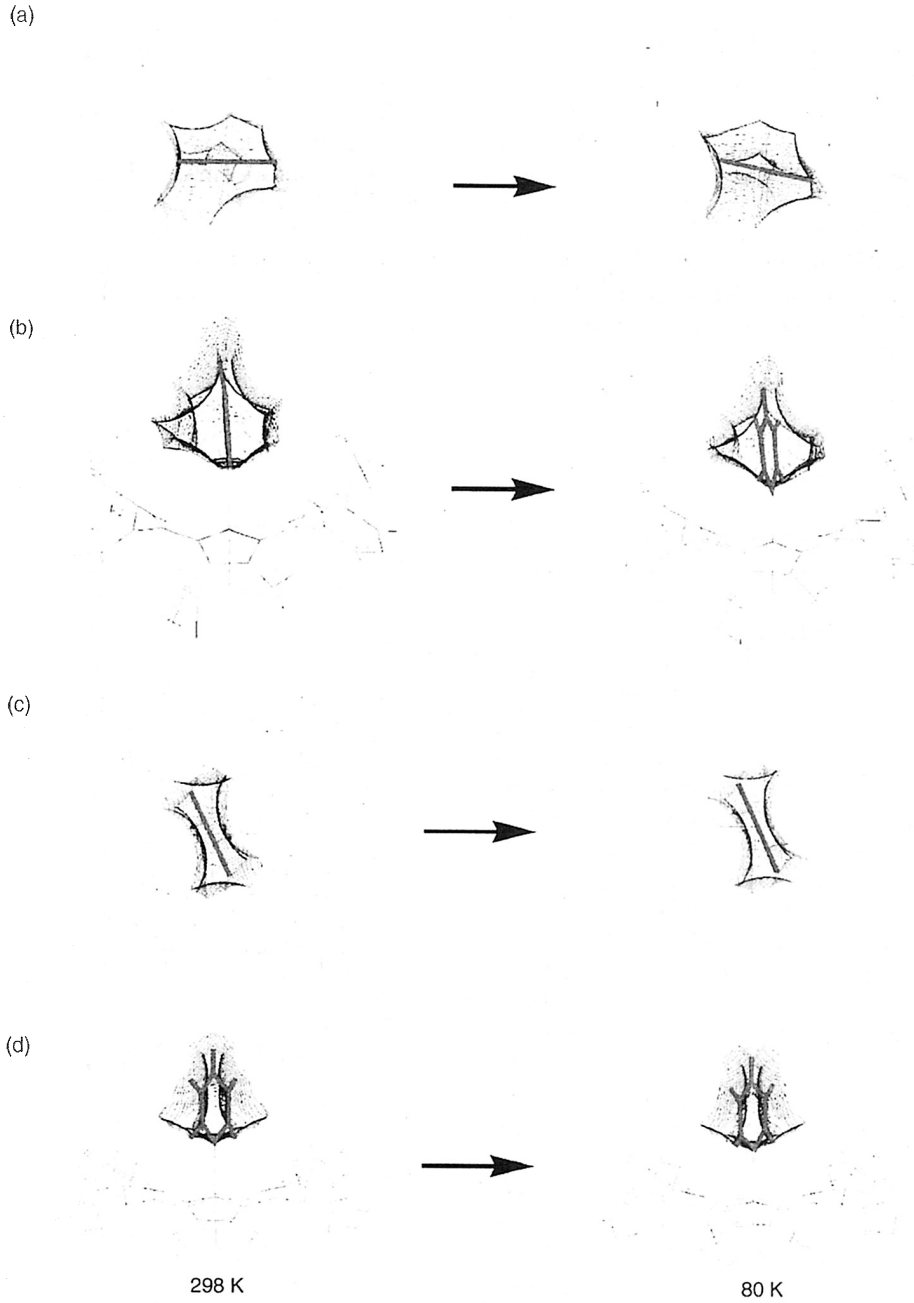

Fig. 25. The spatial environment around the axial ligands. (a) and (b) $[Fe(OETPP)Py_2]^+$ viewed along the heme normal and along the N2–N4 axis, respectively, (c) and (d) $[Fe(OMTPP)Py_2]^+$ viewed along the normal to the average plane and along the N2–N4 axis, respectively. Coordinated pyridine is drawn by the red bald lines. Adapted from Ref. [77].

even at ambient temperature. As a result, the spin crossover process, which requires the decrease in the $Fe–N_{axial}$ bond length caused by the contraction of the unit cell, takes place only in $[Fe(OETPP)Py_2]^+$ [77,129].

Fig. 25 shows the spatial environment around the axial ligands of $[Fe(OETPP)Py_2]^+$ and $[Fe(OMTPP)Py_2]^+$ at 298 and 80 K determined by CAVITY calculation developed by Ohashi et al. [130,131]. The cavity sizes around the pyridine ligand listed in Table 13 are quite different between two complexes. The OETPP complex showing a spin-crossover phenomenon has cavities of 32.08 and 28.88 $Å^3$ at 298 K, while the OMTPP complex has much smaller cavity, 19.81 $Å^3$. Thus, the cavity around the pyridine ligand in $[Fe(OMTPP)Py_2]^+$ is only 65% of that in $[Fe(OETPP)Py_2]^+$. Close inspection of the cavities in Fig. 25(a) and (b) reveals that the pyridine ligand in the OETPP complex, signified as a red bold line, aligns along the diagonal N1–N3 axis and makes contact with a convex surface created by the neighboring atoms at 298 K. When the temperature is lowered to 80 K, the $Fe–N_{axial}$ bond contracts. Concomitantly, the pyridine ligand rotates toward the diagonal $C_{meso}–C_{meso}$ axis to

minimize the repulsion with the porphyrin core until it makes contact with another convex surface. In other words, each pyridine ligand of $[Fe(OETPP)Py_2]^+$ has a room for rotation, which in turn enables the contraction of the $Fe–N_{axial}$ bond and makes the spin crossover possible. In contrast, the pyridine ligand in $[Fe(OMTPP)Py_2]^+$ is placed in a densely packed crystal lattice even at room temperature and that the axial ligands are confined in the narrow cavities as shown in Fig. 25(c) and (d). In other words, the loosely packed crystal system and the wide cavities around the axial ligands to allow their displacement and rotation are the important requirements for the spin transition to occur in the solid state [80].

5. Conclusions

Effects of porphyrin deformation on the electronic structures of iron(III) porphyrinates have been reviewed. In the case of low-spin ($S=1/2$) complexes with ruffled porphyrin ring, the interaction between the iron d_{xy} and porphyrin a_{2u} orbitals raises the energy level of the iron d_{xy} orbital. As a result, the low-spin complexes tend to adopt the less common $(d_{xz}, d_{yz})^4(d_{xy})^1$ ground state. Deformation of the porphyrin ring also affects the spin state of iron(III) porphyrinates. Thus, the complexes with a highly deformed porphyrin ring tend to stabilize the intermediate-spin ($S=3/2$) state if they have axial ligands with weak field strengths. In fact, highly ruffled $Fe(T^iPrP)ClO_4$ and $[Fe(T^iPrP)(THF)_2]ClO_4$ as well as highly saddled $Fe(OETPP)ClO_4$ and $[Fe(OETPP)(THF)_2]ClO_4$ adopt an essentially pure intermediate-spin ($S=3/2$) state. The results are in sharp contrast to the case of $Fe(TPP)ClO_4$ and $[Fe(TPP)(THF)_2]^+$, which adopt not a pure $S=3/2$ but the spin admixture of the $S=5/2$ and $S=3/2$. Ruffled T^iPrP and saddled OETPP cores exhibit, however, a sharp difference if the axial ligands are nitrogen bases with weak field strength. While ruffled $[Fe(T^iPrP)(4\text{-}CNPy)_2]^+$ shows the low-spin state with a quite pure $(d_{xz}, d_{yz})^4(d_{xy})^1$ ground state, saddled $[Fe(OETPP)(4\text{-}CNPy)_2]^+$ adopts an essentially pure intermediate-spin state. Thus, the spin state of $[Fe(OETPP)L_2]^+$ changes from the $S=1/2$ to the $S=3/2$ as the field strengths of nitrogen bases are weakened, i.e. from DMAP to Py, and then to 4-CNPy. The complex carrying axial ligand with medium field strength such as $[Fe(OETPP)Py_2]^+$, therefore, shows a spin crossover from the $S=3/2$ to the $S=1/2$ both in solution and in the solid as the temperature is lowered.

Acknowledgments

The author would like to thank his current and former coworkers and students who have significantly contributed to the work reported from this laboratory that is referenced in this review. First of all, the author thanks Dr. Yoshiki Ohgo, Dr. Akira Ikezaki, and Dr. Takahisa Ikeue. Without their contribution, the work would never have been accomplished. The author also thanks to Prof. Masashi Takahashi and Prof. Masuo Takeda of Toho University for helpful discussion and measurement of Mössbauer spectra, to Prof. Saburo Neya of Chiba University and Prof. M. Graça H. Vicente of Louisiana State University for synthetic assistance, to Prof. Gérard Simonneaux of Université de Rennes 1 for valuable discussion on heme electronic structure, to Prof. Yuji Ohashi and Prof. Hidehiro Uekusa of Tokyo Institute of Technology for the assistance of X-ray crystallographic measurements, to Prof. Hiroshi Fujii and Mr. Masahiro Sakai of Institute for Molecular Science (IMS) for the assistance of EPR and SQUID measurements. This work was supported by the Grant in Aid for Scientific Research from Ministry of Education, Culture, Sports, Science and Technology, Japan.

References

[1] E.I. Solomon, A.B.P. Lever (Eds.), Inorganic Electronic Structure and Spectroscopy, vol. 1, John Wiley & Sons, Inc., New York, 1999.
[2] G.N. La Mar, F.A. Walker, in: D. Dolphin (Ed.), The Porphyrin, vol. IV, Academic Press, New York, 1999 (Chapter 2).
[3] F.A. Walker, in: K.M. Kadish, K.M. Smith, R. Guilard (Eds.), The Porphyrin Handbook, vol. 5, Academic Press, San Diego, 2000 (Chapter 36).
[4] F.A. Walker, Inorg. Chem. 42 (2003) 4526.
[5] F.A. Walker, Chem. Rev. 104 (2004) 589.
[6] H.M. Goff, in: A.B.P. Lever, H.B. Gray (Eds.), Physical Bioinorganic Chemistry Series 1: Iron Porphyrin, I, Nuclear Magnetic Resonance of Iron Porphyrins, Addison-Wesley, Reading, MA, 1983, p. 237.
[7] F.A. Walker, U. Simonis, in: L.J. Berliner, J. Reuben (Eds.), NMR of Paramagnetic Molecules, vol. 12, Plenum Press, New York, 1993, p. 133.
[8] I. Bertini, C. Luchinat, in: A.B.P. Lever (Ed.), NMR of Paramagnetic Substances, Coordination Chemistry Reviews, vol. 150, Elsevier, Amsterdam, 1996, p. 29.
[9] I. Bertini, C. Luchinat, in: A.B.P. Lever, H.B. Gray (Eds.), NMR of Paramagnetic Molecules in Biological Systems, Physical Bioinorganic Chemistry Series, vol. 3, Benjamin/Bummings, Menlo Park, 1986, p. 165.
[10] M.O. Senge, in: K.M. Kadish, K.M. Smith, R. Guilard (Eds.), The Porphyrin Handbook, vol. 1, Academic Press, San Diego, CA, 2000, p. 239 (Chapter 6).
[11] J.A. Shelnutt, in: K.M. Kadish, K.M. Smith, R. Guilard (Eds.), The Porphyrin Handbook, vol. 7, Academic Press, San Diego, CA, 2000, p. 167 (Chapter 50).
[12] A. Ghosh, E. Gonzalez, T. Vangberg, J. Phys. Chem. B 103 (1999) 1363.
[13] R.-J. Cheng, P.-Y. Chen, Chem. Eur. J. 5 (1999) 1708.
[14] R.-J. Cheng, P.-Y. Chen, T. Lovell, T. Liu, L. Noodleman, D.A. Case, J. Am. Chem. Soc. 125 (2003) 6774.
[15] R.-J. Cheng, Y.-K. Wang, P.-Y. Chen, Y.-P. Han, C.-C. Chang, Chem. Commun. (2005) 1312.
[16] J.A. Shelnutt, X.-Z. Song, J.-G. Ma, S.-L. Jia, W. Jentzen, C.J. Medforth, J. Chem. Soc. Rev. 27 (1998) 31.
[17] J.-G. Ma, J. Zhang, R. Franco, S.-L. Jia, I. Moura, J.G. Moura, P.M.H. Kroneck, J.A. Shelnutt, Biochemistry 37 (1998) 12431.
[18] G.W. Bushnell, G.V. Louie, G.D. Brayer, J. Mol. Biol. 24 (1990) 585.
[19] N. Kunishima, K. Fukuyama, H. Matsubara, H. Hatanaka, Y. Shibano, T. Amachi, J. Mol. Biol. 235 (1994) 344.
[20] J.D. Hobbs, J.A. Shelnutt, J. Protein Chem. 14 (1995) 19.
[21] G.N. La Mar, J.D. Satterlee, J.S. de Ropp, in: K.M. Kadish, K.M. Smith, R. Guilard (Eds.), The Porphyrin Handbook, vol. 5, Academic Press, San Diego, CA, 2000, p. 185 (Chapter 37).
[22] G. Simonneaux, A. Bondon, in: K.M. Kadish, K.M. Smith, R. Guilard (Eds.), The Porphyrin Handbook, vol. 5, Academic Press, San Diego, CA, 2000, p. 299 (Chapter 38).
[23] L. Banci, I. Bertini, C. Luchinat, P. Turano, in: K.M. Kadish, K.M. Smith, R. Guilard (Eds.), The Porphyrin Handbook, vol. 5, Academic Press, San Diego, CA, 2000, p. 323 (Chapter 37).
[24] W. Jentzen, M.C. Simpson, J.D. Hobbs, X. Song, T. Ema, N.Y. Nelson, C.J. Medforth, K.M. Smith, M. Veyrat, M. Mazzanti, R. Ramasseul,

J.-C. Marchon, T. Takeuchi, E.A. Goddard III, J.A. Shelnutt, J. Am. Chem. Soc. 117 (1995) 11085.
[25] M.O. Senge, T. Ema, K.M. Smith, J. Chem. Soc., Chem. Commun. 733 (1995).
[26] M. Veyrat, R. Ramasseul, J.-C. Marchon, I. Turowska-Tyrk, W.R. Schiedt, N. J. Chem. 19 (1995) 1199.
[27] M.O. Senge, I. Bischoff, N.Y. Nelson, K.M. Smith, J. Porphyrins Phthalocyanines 3 (1999) 99.
[28] K.M. Barkigia, L. Chantranupong, K.M. Smith, J. Fajer, J. Am. Chem. Soc. 110 (1988) 7566.
[29] K.M. Barkigia, M.D. Berber, J. Fajer, C.J. Medforth, M.W. Renner, K.M. Smith, J. Am. Chem. Soc. 112 (1990) 8851.
[30] C.J. Medforth, M.O. Senge, K.M. Smith, L.D. Sparks, J.A. Shelnutt, J. Am. Chem. Soc. 114 (1992) 9859.
[31] M.K. Safo, G.P. Gupta, C.T. Watson, U. Simonis, F.A. Walker, W.R. Scheidt, J. Am. Chem. Soc. 114 (1992) 7066.
[32] M.K. Safo, F.A. Walker, A.M. Raitsimring, W.P. Walters, D.P. Dolata, P.G. Debrunner, W.R. Scheidt, J. Am. Chem. Soc. 116 (1994) 7760.
[33] M.R. Cheesman, F.A. Walker, J. Am. Chem. Soc. 118 (1996) 7373.
[34] G.N. La Mar, J.D. Gaudio, J.S. Frye, Biochim. Biophys. Acta 498 (1977) 422.
[35] G. Simonneaux, F. Hindre, M. Le Plouzennec, Inorg. Chem. 28 (1989) 823.
[36] C. Geze, N. Legrand, A. Bondon, G. Simonneaux, Inorg. Chim. Acta 195 (1992) 73.
[37] F.A. Walker, H. Nasri, I. Turowska-Tyrk, K. Mohanrao, C.T. Watson, N.V. Shokhirev, P.G. Debrunner, W.R. Scheidt, J. Am. Chem. Soc. 118 (1996) 12109.
[38] M.-A. Pilard, M. Guillemot, L. Toupet, J. Jordanov, G. Simonneaux, Inorg. Chem. 36 (1997) 6307.
[39] G. Simonneaux, V. Schünemann, C. Morice, L. Carel, L. Toupet, H. Winkler, A.X. Trautwein, F.A. Walker, J. Am. Chem. Soc. 122 (2000) 4366.
[40] W.R. Scheidt, C.A. Reed, Chem. Rev. 81 (1981) 543.
[41] W.R. Scheidt, Y.J. Lee, Struct. Bonding (Berlin) 64 (1987) 1.
[42] W.R. Scheidt, in: K.M. Kadish, K.M. Smith, R. Guilard (Eds.), The Porphyrin Handbook, vol. 3, Academic Press, San Diego, CA, 2000, p. 49 (Chapter 16).
[43] T. Ikeue, Y. Ohgo, T. Saitoh, M. Nakamura, H. Fujii, M. Yokoyama, J. Am. Chem. Soc. 122 (2000) 4068.
[44] A. Ikezaki, T. Ikeue, M. Nakamura, Inorg. Chim. Acta 335 (2002) 91.
[45] M. Nakamura, T. Ikeue, H. Fujii, T. Yoshimura, J. Am. Chem. Soc. 119 (1997) 6284.
[46] M. Nakamura, T. Ikeue, H. Fujii, T. Yoshimura, K. Tajima, Inorg. Chem. 37 (1998) 2405.
[47] T. Ikeue, Y. Ohgo, T. Saitoh, T. Yamaguchi, M. Nakamura, Inorg. Chem. 40 (2001) 3423.
[48] S. Wolowiec, L. Latos-Grazynski, M. Mazzanti, J.-C. Marchon, Inorg. Chem. 36 (1997) 5761.
[49] S. Wolowiec, L. Latos-Grazynki, D. Toronto, J.-C. Marchon, Inorg. Chem. 37 (1998) 724.
[50] K.T. Moore, J.T. Fletcher, M.J. Therien, J. Am. Chem. Soc. 121 (1999) 5196.
[51] Y. Ohgo, T. Ikeue, M. Nakamura, Acta Crystallogr., Sect. C 55 (1999) 1817.
[52] Y. Ohgo, et al., unpublished result.
[53] T. Ikeue, Y. Ohgo, A. Uchida, M. Nakamura, H. Fujii, M. Yokoyama, Inorg. Chem. 38 (1999) 1276.
[54] Y. Ohgo, T. Ikeue, T. Saitoh, M. Nakamura, Chem. Lett. 42 (2002).
[55] W.R. Scheidt, S.R. Osvath, Y.J. Lee, J. Am. Chem. Soc. 109 (1987) 1958.
[56] O.Q. Munro, H.M. Marques, P.G. Debrunner, K. Mohanrao, W.R. Scheidt, J. Am. Chem. Soc. 117 (1995) 935.
[57] M. Nakamura, K. Tajima, K. Tada, K. Ishizu, N. Nakamura, Inorg. Chem. Acta 24 (1994) 113.
[58] M. Nakamura, N. Nakamura, Chem. Lett. (1991).
[59] A. Ikezaki, M. Nakamura, J. Inorg. Biochem. 84 (2001) 137.
[60] G.A. Caignan, R. Deshmukh, Y. Zeng, A. Wilks, R.A. Bunce, M. Rivera, J. Am. Chem. Soc. 125 (2003) 11842.
[61] M. Rivera, G.A. Caignan, Anal. Bioanal. Chem. 378 (2004) 1464.
[62] P. Turner, M.J. Gunter, Inorg. Chem. 33 (1994) 1406.
[63] H.M. Goff, J. Am. Chem. Soc. 103 (1981) 3714.
[64] J. Mao, Y. Zhang, E. Oldfield, J. Am. Chem. Soc. 124 (2002) 13911.
[65] M. Karplus, G.K. Fraenkel, J. Chem. Phys. 35 (1961) 1312.
[66] E.T. Strom, G.R. Underwood, D. Jurkowitz, Mol. Phys. 24 (1972) 901.
[67] M. Nakamura, A. Hoshino, A. Ikezaki, T. Ikeue, Chem. Commun. (2003).
[68] H. Fujii, J. Am. Chem. Soc. 124 (2002) 5036.
[69] H. Goff, J. Am. Chem. Soc. 99 (1977) 7723.
[70] M. Hada, J. Am. Chem. Soc. 126 (2004) 486.
[71] S. Ghosh, E. Gonzalez, T. Vangberg, J. Phys. Chem. B 103 (1999) 1363.
[72] C.P.S. Taylor, Biochim. Biophys. Acta 491 (1977) 137.
[73] T.L. Bohan, J. Magn. Reson. 26 (1977) 109.
[74] G. Palmer, in: A.B.P. Lever, H.B. Gray (Eds.), Iron Porphyrins, Part II: Physical Bioinorganic Chemistry Series 2, Addison-Wesley, Reading, MA, 1983, p. 43.
[75] M.K. Safo, G.P. Gupta, F.A. Walker, W.R. Scheidt, J. Am. Chem. Soc. 113 (1991) 5497.
[76] T. Ikeue, T. Yamaguchi, Y. Ohgo, M. Nakamura, Chem. Lett. 342 (2000).
[77] Y. Ohgo, T. Ikeue, M. Takahashi, M. Takeda, M. Nakamura, Eur. J. Inorg. Chem. 798 (2004).
[78] H. Ogura, L. Yatsunyk, C.J. Medforth, K.M. Smith, K.M. Barkigia, M.W. Renner, D. Melamed, F.A. Walker, J. Am. Chem. Soc. 123 (2001) 6564.
[79] L.A. Yatsunyk, M.D. Carducci, F.A. Walker, J. Am. Chem. Soc. 125 (2003) 15986.
[80] A. Ikezaki, M. Nakamura, Inorg. Chem. 41 (2002) 2761.
[81] M. Rivera, G.A. Caignan, A.V. Astashkin, A.M. Raitsimring, T.K. Shokhireva, F.A. Walker, J. Am. Chem. Soc. 124 (2002) 6077.
[82] Y. Zeng, G.A. Caignan, R.A. Bunce, J.C. Rodriguez, A. Wilks, M. Rivera, J. Am. Chem. Soc. 127 (2005) 9794.
[83] M.M. Maltempo, T.H. Moss, M.A. Cusanovich, Biochim. Biophys. Acta 342 (1974) 290.
[84] C.A. Reed, T. Mashiko, S.P. Bentley, M.E. Kastner, W.R. Scheidt, K. Spartalian, G. Lang, J. Am. Chem. Soc. 101 (1979) 2948.
[85] A.D. Boersma, H.M. Goff, Inorg. Chem. 21 (1982) 581.
[86] C.A. Reed, F. Guiset, J. Am. Chem. Soc. 118 (1996) 3281.
[87] D.R. Evans, C.A. Reed, J. Am. Chem. Soc. 122 (2000) 4660.
[88] K. Rachlewicz, L. Latos-Grazynski, E. Vogel, Z. Ciunik, L.B. Jerzykiewicz, Inorg. Chem. 41 (2002) 1979.
[89] Y. Ohgo, S. Neya, T. Ikeue, M. Takahashi, M. Takeda, N. Funasaki, M. Nakamura, Inorg. Chem. 41 (2002) 4627.
[90] T. Ikeue, Y. Ohgo, M. Takahashi, M. Takeda, S. Neya, N. Funasaki, M. Nakamura, Inorg. Chem. 40 (2001) 3650.
[91] M. Zobrist, G.N. La Mar, J. Am. Chem. Soc. 100 (1978) 1944.
[92] A. Hoshino, M. Nakamura, Chem. Lett. 33 (2004) 1234.
[93] A. Hoshino, Y. Ohgo, M. Nakamura, Inorg. Chem. 44 (2005) 7333.
[94] G.E. Toney, L.W. terHaar, J.E. Savrin, A. Gold, W.E. Hatlfield, R. Sangaiah, Inorg. Chem. 23 (1984) 2561.
[95] G.E. Toney, A. Gold, J.E. Savrin, L.W. terHaar, R. Sangaiah, Inorg. Chem. 23 (1984) 4350.
[96] M.J. Nesset, S. Cai, T.K. Shokhirieva, M.V. Shokhirev, S.E. Jacobson, K. Jayaraj, A. Gold, F.A. Walker, Inorg. Chem. 39 (2000) 532.
[97] T. Sakai, Y. Ohgo, A. Hoshino, T. Ikeue, T. Saitoh, M. Takahashi, M. Nakamura, Inorg. Chem. 43 (2004) 5034.
[98] Y. Ohgo, S. Neya, M. Takahashi, M. Takeda, N. Funasaki, M. Nakamura, Chem. Lett. 32 (2003) 526.
[99] A. Ikezaki, M. Nakamura, Inorg. Chem. 41 (2002) 6225.
[100] S. Fujii, T. Yoshimura, H. Kamada, K. Yamaguchi, S. Suzuki, S. Shidara, S. Takakuwa, Biochim. Biophys. Acta 1251 (1995) 161.
[101] G.N. La Mar, J.T. Jackson, L.B. Dugad, M.A. Cusanovich, R.G.I. Bartsch, J. Biol. Chem. 265 (1990) 16173.

[102] J.-P. Simonato, J. Pecaut, L.L. Pape, J.-L. Oddou, C. Jeandey, M. Shang, W.R. Scheidt, J. Wojacynski, S. Wolowiec, L. Latos-Grazynski, J.-C. Marchon, Inorg. Chem. 39 (2000) 3978.
[103] T. Ikeue, T. Saitoh, T. Yamaguchi, Y. Ohgo, M. Nakamura, M. Takahashi, M. Takeda, Chem. Commun. (1989) 2000.
[104] T. Sakai, Y. Ohgo, T. Ikeue, M. Takahashi, M. Takeda, M. Nakamura, J. Am. Chem. Soc. 125 (2003) 13028.
[105] Y. Ohgo, T. Saitoh, M. Nakamura, Acta. Crystallogr. C57 (2001) 233.
[106] B. Cheng, M.K. Safo, R.D. Orosz, C.A. Reed, P.G. Debrunner, W.R. Scheidt, Inorg. Chem. 33 (1994) 1319.
[107] B.R. Serr, C.E.L. Headford, O.P. Anderson, C.M. Elliot, K. Spartalian, V.E. Fainzilberg, W.E. Hatfield, B.R. Rohrs, S.S. Eaton, G.R. Eaton, Inorg. Chem. 31 (1992) 5450.
[108] J. Shao, E. Steene, B.M. Hoffman, A. Ghosh, Eur. J. Inorg. Chem. 1609 (2005).
[109] A. Ghosh, I. Halvorsen, H.J. Nilsen, E. Steene, T. Wondimagegn, R. Lie, E. van Caemelbecke, N. Guo, Z. Ou, K.M. Kadish, J. Phys. Chem. B. 105 (2001) 8120.
[110] M.W. Renner, K.M. Barkigia, Y. Zhang, C.J. Medforth, K.M. Smith, J. Fajer, J. Am. Chem. Soc. 116 (1994) 8582.
[111] M. Nakamura, T. Ikeue, Y. Ohgo, M. Takahashi, M. Takeda, Chem. Commun. 1198 (2002).
[112] K.M. Barkigia, M.W. Renner, J. Fajer, J. Porphyrins Phthalocyanins 5 (2001) 415.
[113] R.-J. Cheng, P.-Y. Chen, P.-R. Gau, C.-C. Chen, S.-M. Peng, J. Am. Chem. Soc. 119 (1997) 2563.
[114] V. Schünemann, M. Gerdan, A.X. Trautwein, N. Haoudi, D. Mandon, J. Fischer, R. Weiss, A. Tabard, R. Guilard, Angew. Chem., Int. Ed. 38 (1999) 3181.
[115] W.R. Scheidt, D.K. Geiger, K.J. Haller, J. Am. Chem. Soc. 104 (1982) 495.
[116] M.K. Ellison, H. Narsi, Y.-M. Xia, J.-C. Marchon, C.E. Schulz, P.G. Debrunner, W.R. Scheidt, Inorg. Chem. 36 (1997) 4804.
[117] S. Neya, M. Tsubaki, H. Hori, T. Yonetani, N. Funasaki, Inorg. Chem. 40 (2001) 1220.
[118] S. Neya, C.K. Chang, D. Okuno, Y. Hoshino, M. Hata, N. Funasaki, Inorg. Chem. 44 (2005) 1193.
[119] T. Ikeue, Y. Ohgo, T. Yamaguchi, M. Takahashi, M. Takeda, M. Nakamura, Angew. Chem. Int. Ed. 40 (2001) 2617.
[120] E.T. Kintner, J.H. Dawson, Inorg. Chem. 30 (1991) 4892.
[121] T. Ikeue, Y. Ohgo, O. Ongayi, G.H. Vicente, M. Nakamura, Inorg. Chem. 42 (2003) 5560.
[122] D.F. Evans, T.A. James, J. Chen. Soc. (1979) 723.
[123] W.O. Koch, V. Schünemann, M. Gerdan, A.X. Trautwein, H.-J. Krüger, Chem. Eur. J. 4 (1998) 686.
[124] H. Chun, E. Bill, T. Weyhermuller, K. Wieghardt, Inorg. Chem. 42 (2003) 5612.
[125] L.A. Yatsunyk, F.A. Walker, Inorg. Chem. 43 (2004) 4341.
[126] J.R. Sams, T.B. Tsin, in: D. Dolphin (Ed.), The Porphyrins, vol. 4, Academic Press, New York, 1979 (Chapter 9).
[127] P.G. Debrunner, in: A.B.P. Lever, H.B. Gray (Eds.), Iron Porphyrin Part III, VCH, New York, 1989, p. 139.
[128] P. Gütlich, J. Ensling, in: E.I. Solomon, A.B.P. Lever (Eds.), Inorganic Electronic Structure and Spectroscopy, vol. 1, John Wiley & Sons, Inc., New York, 1999, p. 161.
[129] Y. Ohgo, T. Ikeue, M. Nakamura, Inorg. Chem. 41 (2002) 1698.
[130] Y. Ohashi, K. Yanagi, T. Kurihara, Y. Sasada, Y. Ohgo, J. Am. Chem. Soc. 103 (1981) 5805.
[131] A. Uchida, Y. Ohashi, Y. Sasada, Nature (London) 320 (1986) 51.

Novel spin transition between S = 5/2 and S = 3/2 in highly saddled iron(III) porphyrin complexes at extremely low temperatures†

Yoshiki Ohgo,*[ab] Yuya Chiba,[c] Daisuke Hashizume,[d] Hidehiro Uekusa,[e] Tomoji Ozeki[e] and Mikio Nakamura*[abf]

Received (in Cambridge, UK) 30th January 2006, Accepted 14th March 2006
First published as an Advance Article on the web 28th March 2006
DOI: 10.1039/b601412g

A novel spin transition between S = 5/2 and S = 3/2 has been observed for the first time in five-coordinate, highly saddled iron(III) porphyrinates by EPR and SQUID measurements at extremely low temperatures.

A wide variety of research has been carried out on the spin transition in naturally occurring heme proteins because of their relevance to the important functional tuning process.[1] For example, the ferrihemes in cytochrome P450 adopt the low-spin (S = 1/2) in the resting state. However, the spin transition to the high-spin state (S = 5/2) occurs on binding the organic substrate, which triggers the one-electron reduction to proceed the catalytic oxidation reaction.[2] The spin transition between S = 5/2 and S = 1/2 has also been studied in model complexes such as $[Fe(OEP)(3\text{-}ClPy)_2]^+$.[3,4] In contrast to high-spin and low-spin states, the intermediate-spin state (S = 3/2) is quite rare.[5] Reed and Guiset reported that [Fe(TPP)]X is in an essentially pure intermediate-spin state if the axial anionic ligand X is extremely weak, $[Ag(Br_6CB_{11}H_6)_2]^-$.[6] Ourselves and others have also reported that highly saddled porphyrins such as $[Fe(OETPP)L_2]ClO_4$, and core-contracted porphycenes and corroles such as $[Fe(TPrPc)L_2]ClO_4$ and $[Fe(TPFC)L_2]$ adopt a quite pure intermediate-spin state if the field strengths of the axial ligands are fairly weak.[7] Furthermore, the saddled complex with a much stronger pyridine (Py) ligand, $[Fe(OETPP)(Py)_2]^+$, exhibits a novel spin transition between S = 3/2 and S = 1/2.[8] Occurrence of a similar spin transition has recently been reported by Rivera and Caignan in the heme metabolism process mediated by human heme oxygenase.[9] While the spin transitions between S = 5/2 and S = 1/2, and between S = 3/2 and S = 1/2 have been observed both in heme proteins and model heme complexes, the spin transition between S = 5/2 and S = 3/2 has never been observed before. In fact, the mixed S = 5/2 and S = 3/2 spin state is considered to be a quantum mechanical spin admixture

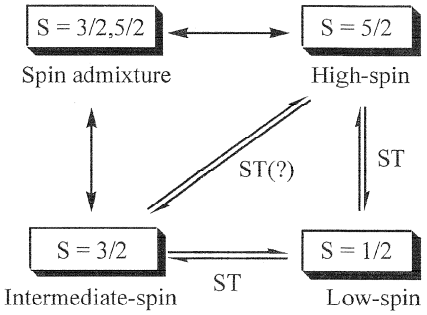

Scheme 1 Possible spin transitions (ST) in iron(III) porphyrinates.

caused by the spin–orbit coupling between S = 3/2 and S = 5/2 states (Scheme 1).[10] In the course of our studies on the spin transition in highly saddled complexes, we found that structurally similar complexes $[Fe(OMTArP)(H_2O)]ClO_4$ (**1** and **2**), shown in Scheme 2, serve an unprecedented example showing the spin transition between S = 3/2 and S = 5/2 spin states.

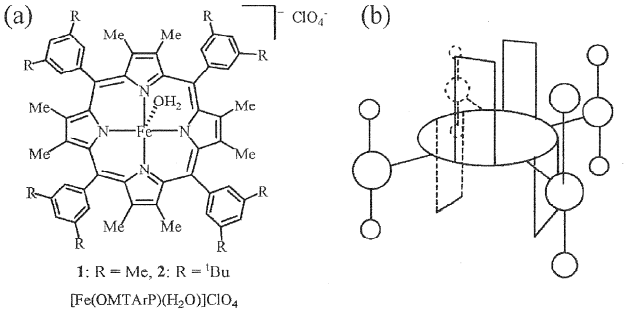

Scheme 2 (a) Complexes **1** and **2** examined in this study, and (b) a schematic drawing of them.

Complexes **1** and **2** were prepared by the condensation reactions between 3,4-dimethylpyrrole and 3,5-dimethylbenzaldehyde/3,5-di-*tert*-butylbenzaldehyde, followed by the insertion of iron using $FeCl_2 \cdot 4H_2O$ in DMF, and then by the addition of a benzene solution of $AgClO_4$.[11] ^1H NMR (CD_2Cl_2, 298 K): **1** δ = 60.1 (pyrrole-CH_3), 3.78 (*meta*-CH_3), 11.7 (*ortho*-H) and 9.17 (*para*-H); **2** δ = 60.4 (pyrrole-CH_3), 11.7 (*ortho*-H) and 9.12 (*para*-H). The large downfield shift of the pyrrole-CH_3, as well as of the *ortho*- and *para*-H signals, suggests that these complexes are in the intermediate-spin state at ambient temperature.[12]

[a]*Department of Chemistry, School of Medicine, Toho University, Ota-ku, Tokyo 143-8540, Japan. E-mail: yohgo@med.toho-u.ac.jp; mnakamu@med.toho-u.ac.jp*
[b]*Research Center for Materials with Integrated Properties, Toho University, Funabashi 274-8510, Japan*
[c]*Division of Biomolecular Science, Graduate School of Science, Toho University, Funabashi 274-8510, Japan*
[d]*Molecular Characterization Team, RIKEN, Wako, Saitama 351-0198, Japan*
[e]*Department of Chemistry and Materials Science, Tokyo Institute of Technology, Tokyo 152-8551, Japan*
[f]*Division of Chemistry, Graduate School of Science, Toho University, Funabashi 274-8510, Japan*
† Electronic Supplementary Information (ESI) available: Temperature dependent EPR spectra, crystal structure discussion and crystal packing diagrams. See DOI: 10.1039/b601412g

This journal is © The Royal Society of Chemistry 2006

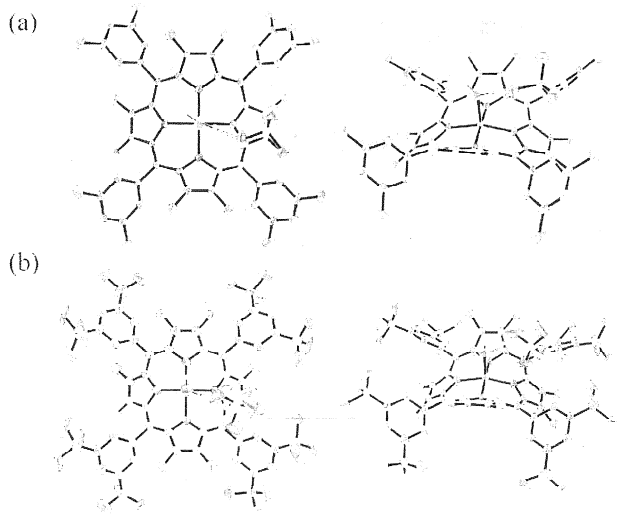

Fig. 1 Molecular structures of (a) **1** and (b) **2**. Ellipsoids are colored in grey (carbon), blue (nitrogen), red (oxygen), green (chlorine), cyan (hydrogen) and magenta (iron). Hydrogen bonds are shown as dotted lines.

At first, we expected that the complexes obtained should be [Fe(OMTArP)]ClO_4. However, the X-ray crystallographic analysis shown in Fig. 1 has revealed that both **1** and **2** are highly saddled five-coordinated mono(aqua) complexes.[13,14] Fig. 2 shows the perpendicular displacement of the peripheral carbon atoms. The maximum deviations from the least-squares plane are 1.32–1.35 Å, which are seen in the pyrrole β-carbons for both complexes. Thus, these complexes can be classified into the group of those that have a severely saddled porphyrin ring.[16] Table 1 lists some geometric parameters of **1** and **2**, together with those of some analogous complexes.

Temperature dependent EPR spectra of **1** and **2** have been acquired both in frozen CH_2Cl_2 solution and in the solid state. Parts of them are given in Fig. 3. Each complex shows a similar spectral change in both solution and the solid state. The EPR spectra at 4 K exhibit two types of signals characteristic of high-spin and intermediate-spin species.[17] The g values, determined by computer simulations of the observed spectra, are as follows: **1**, 6.10, 5.90, 2.00 (S = 5/2), and 4.20, 3.80, 2.10 (S = 3/2); **2**, 6.10, 5.90, 2.00 (S = 5/2), and 4.37, 3.77, 1.99 (S = 3/2). To our great surprise, the signal intensities for the intermediate-spin species increased while those for the high-spin species decreased as the temperature was raised. Thus, both **1** and **2** exist exclusively as the

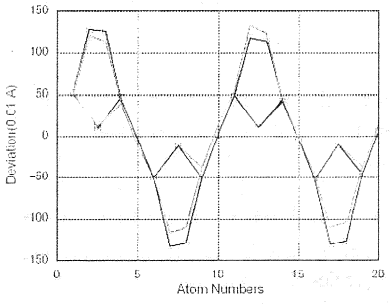

Fig. 2 Perpendicular displacement of 24 peripheral atoms from the N4 mean plane: ○(red), **1**; □(black), **2**.

Table 1 Comparison of various geometric parameters in five-coordinated saddle-shaped iron(III) porphyrin complexes

Complex	Fe–N_p/ Å[a]	Fe–X_{ax}/ Å[b]	ΔFe/ Å[c]	N4 area/ Å^2[d]	S[e]	Ref.
1	1.946(4)	2.084(4)	0.285(2)	7.45	3/2	This work
2	1.960(2)	2.056(2)	0.232(1)	7.59	3/2	This work
Fe(OMTPP)Cl	2.034	2.247	0.464	7.87	5/2	15
Fe(OETPP)Cl	2.030	2.242	0.467	7.83	5/2	15
Fe(OETPP)ClO_4	1.963	2.059	0.262	7.59	3/2	7*b*

[a] Bond length between the iron and the pyrrole nitrogen. [b] Bond length between the iron and the axial ligand. [c] Out-of-plane deviation of the iron(III) ion from the N_4 plane. [d] The area of the plane consisting of the four nitrogen atoms of the pyrrole rings. [e] Spin state at ambient temperature.

intermediate-spin species above 70 K. This process turns out to be reversible because the original spectra were observed when the temperature was lowered back to 4 K. The temperature dependence of the EPR spectra could best be explained in terms of the spin transition between S = 5/2 and S = 3/2. It should be noted that, while **2** shows an almost complete spin transition between S = 3/2 and S = 5/2, **1** exists mainly as the intermediate-spin species throughout the temperature range examined. The population of each species has been determined by computer simulation of the observed spectra. The van't Hoff plots yield ΔH° and ΔS° values, corresponding to the equilibrium given in (eqn. 1), of 60 J mol^{-1} and 48 J mol^{-1} K^{-1} for **1**, and 100 J mol^{-1} and 19 J mol^{-1} K^{-1} for **2**, respectively.

$$\text{high-spin} \underset{}{\overset{K}{\rightleftharpoons}} \text{intermediate-spin} \qquad (1)$$

Fig. 4 shows the correlation of magnetic susceptibility (χ) with $1/T$.

The curved line of **1** almost coincides with that of intermediate-spin Fe(EtioPc)I at higher temperature when $1/T$ is less than 0.05 (or T is higher than 20 K).[18] As $1/T$ becomes larger than 0.05 (or T is lower than 20 K), it starts to deviate from the curved line of Fe(EtioPc)I and approaches that of high-spin Fe(OEP)I. Complex **2** exhibits a similar behavior. These results suggest that the spin transition takes place from the S = 3/2 to the S = 5/2 state as the temperature is lowered below 20 K.

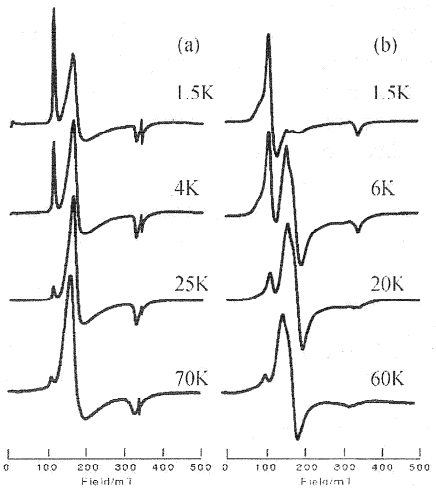

Fig. 3 EPR spectra of (a) **1** taken in frozen CH_2Cl_2 solution and (b) **2** taken in the solid state at various temperatures.

This journal is © The Royal Society of Chemistry 2006

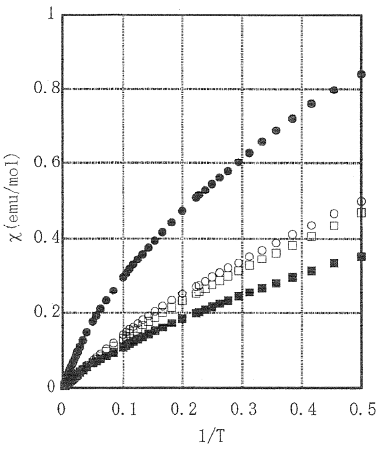

Fig. 4 Correlations between magnetic susceptibility (χ) and inverse temperature ($1/T$). ○, **1**; □, **2**; ●, Fe(OEP)I; ■, Fe(EtioPc)I.

The novel spin transition described above should be ascribable to the unique molecular and crystal structures of **1** and **2**. The data in Table 1 indicate that the out-of-plane deviations of the iron(III) ion, which are signified as ΔFe, are quite different from other saddle-shaped complexes. While the ΔFe values of high-spin complexes are 0.46–0.47 Å, they are only 0.23–0.29 Å in the intermediate-spin complexes. As the temperature is lowered, the unit cell volume is expected to shrink.[19] As **1** and **2** have highly saddled structures with bulky substituents at the porphyrin periphery, as illustrated in Scheme 2, the shrinkage of the unit cell could directly affect each molecule from the lateral side. As a result, the narrow N4 cavities of **1** and **2** could further decrease at extremely low temperature, which could extrude the iron(III) ion away from the N4 plane. The large out-of-plane displacement of the iron(III) ion could stabilize the $d_{x^2-y^2}$ orbital and induce spin transition from the $S = 3/2$ to the $S = 5/2$ state. Needless to say, the X-ray analysis of these complexes at extremely low temperature is clearly necessary to prove the above hypothesis. This now in progress in our laboratory.

In summary, we have found a spin transition between high-spin and intermediate-spin states by EPR spectroscopy and SQUID magnetometry for the first time.

This work was supported by a Research Promotion Grant from Toho University Graduate School of Medicine (no. 05–21 to Y. O.), and by a Grant-in-Aid for Scientific Research from the Ministry of Education, Culture, Sports, Science and Technology, Japan (no. 16550061 to M. N.). Thanks are due to the Research Center for Molecular-Scale Nanoscience, the Institute for Molecular Science (IMS). The synchrotron radiation experiment was performed under the approval of the Photon Factory Program Advisory Committee (proposal no. 2005G021). Thanks are due to Professor Shin-ichi Adachi for his help during the synchrotron radiation experiment.

Notes and references

1 S. J. Lippard and J. M. Berg, in *Principles of Bioinorganic Chemistry*, University Science Books, Mill Valley, CA, 1994.

2 T. L. Poulos, in *The Porphyrin Handbook*, ed. K. M. Kadish, K. M. Smith and R. Guilard, Academic Press, New York, 2000, vol. 4, pp. 189–218.

3 Abbreviations: OEP, TPP, OETPP, TPrPc, TPFC and EtioPc: dianions of 2,3,7,8,12,13,17,18-octaethylporphyrin, 5,10,15,20-tetraphenylporphyrin, 2,3,7,8,12,13,17,18-octaethyl-5,10,15,20-tetraphenylporphyrin, 2,7,12,17-tetrapropylporphycene, 5,10,15-tris(pentafluorophenyl)corrole and 3,6,13,16-tetraethyl-2,7,12,17-tetramethylporphycene, respectively. 3-ClPy: 3-chloropyridine.

4 (*a*) R. W. Scheidt, D. K. Geiger and K. J. Haller, *J. Am. Chem. Soc.*, 1982, **104**, 495; (*b*) S. Neya, M. Tsubaki, H. Hori, T. Yonetani and N. Funasaki, *Inorg. Chem.*, 2001, **40**, 1220.

5 (*a*) D. H. Dolphin, J. R. Sams and T. B. Tsin, *Inorg. Chem.*, 1977, **16**, 711; (*b*) H. Masuda, T. Taga, K. Osaki, H. Sugimoto, Z. Yoshida and H. Ogoshi, *Inorg. Chem.*, 1980, **19**, 950.

6 C. A. Reed and F. Guiset, *J. Am. Chem. Soc.*, 1996, **118**, 3281.

7 (*a*) T. Ikeue, T. Saitoh, T. Yamaguchi, Y. Ohgo, M. Nakamura, M. Takahashi and M. Takeda, *Chem. Commun.*, 2000, 1989; (*b*) K. M. Barkigia, M. W. Renner and J. Fajer, *J. Porphyrins Phthalocyanines*, 2001, **5**, 415; (*c*) M. Nakamura, T. Ikeue, Y. Ohgo, M. Takahashi and M. Takeda, *Chem. Commun.*, 2002, 1198; (*d*) A. Hoshino, Y. Ohgo and M. Nakamura, *Inorg. Chem.*, 2005, **44**, 7333; (*e*) T. Ikeue, Y. Ohgo, M. Takahashi, M. Takeda, S. Neya, N. Funasaki and M. Nakamura, *Inorg. Chem.*, 2001, **40**, 3650; (*f*) K. Rachlewcz, L. Latos-Grażyński, E. Vogel, Z. Ciunik and L. B. Jerzykiewicz, *Inorg. Chem.*, 2002, **41**, 1979; (*g*) L. Simkhovich, I. Goldberg and Z. Gross, *Inorg. Chem.*, 2002, **41**, 5433.

8 (*a*) T. Ikeue, Y. Ohgo, T. Yamaguchi, M. Takahashi, M. Takeda and M. Nakamura, *Angew. Chem., Int. Ed.*, 2001, **40**, 2617; (*b*) Y. Ohgo, T. Ikeue and M. Nakamura, *Inorg. Chem.*, 2002, **41**, 1698.

9 M. Rivera and G. A. Caignan, *Anal. Bioanal. Chem.*, 2004, **378**, 1464.

10 M. M. Maltempo, *J. Chem. Phys.*, 1974, **61**, 2540.

11 K. M. Barkigia, M. D. Berber, J. Fajer, C. J. Medforth, M. W. Renner and K. M. Smith, *J. Am. Chem. Soc.*, 1990, **112**, 8851.

12 (*a*) T. Ikeue, Y. Ohgo, O. Ongayi, M. G. H. Vicente and M. Nakamura, *Inorg. Chem.*, 2003, **42**, 5560; (*b*) SQUID magnetometry has revealed that the effective magnetic moments for **1** and **2** at 300 K are 3.71 μ_B and 3.82 μ_B, respectively.

13 Crystal and molecular structural data for **1**: $C_{60}H_{62}ClFeN_4O_5$, M = 1010.44, orthorhombic, a = 14.4113(3), b = 16.9296(4), c = 21.1176(5) Å, V =5152.2(2) Å^3, T = 110 K, space group $P2_12_12_1$ (no. 19), Z = 4, μ(Mo-K$_\alpha$) = 0.324 mm^{-1}, 53820 reflections measured, 18104 unique (R_{int} = 0.0787) which were used in all calculations. $R(F)$ = 0.0631 ($I > 2\sigma(I)$), 0.0891(all data), $wR(F^2)$ = 0.156 ($I > 2\sigma(I)$), 0.166 (all data), goodness of fit S = 0.941. CCDC 297040. For crystallographic data in CIF or other electronic format see DOI: 10.1039/b601412g. Diffraction data were collected on a Rigaku MERCURY CCD system installed on the NW2 beam line of the Advanced Ring (AR), the Photon Factory (PF) of the High Energy Accelerator Research Organization (KEK) using a 18.00 keV (λ = 0.68878 Å) monochromatized X-ray beam.

14 Crystal and molecular structural data for **2**: $C_{85}H_{112}Cl_3FeN_4O_5$, M = 1415.94, triclinic, a =15.160(4), b = 15.846(4), c = 18.698(5) Å, α = 68.533(7), β = 79.192(9), γ = 83.227(9)°, V = 4100(2) Å^3, T = 298 K, space group P-1 (no. 2), Z = 2, μ(Mo-K$_\alpha$) = 0.331 mm^{-1}, 58762 reflections measured, 17675 unique (R_{int} = 0.16) which were used in all calculations. $R(F)$ = 0.131 ($I > 2\sigma(I)$), 0.22 (all data), $wR(F^2)$ = 0.33 ($I > 2\sigma(I)$), 0.38 (all data), goodness of fit S = 1.039. CCDC 297041. For crystallographic data in CIF or other electronic format see DOI: 10.1039/b601412g.

15 R.-J. Cheng, P.-Y. Chen, P.-R Gau, C.-C. Chen and S.-M. Peng, *J. Am. Chem. Soc.*, 1997, **119**, 2563.

16 M. O. Senge, in *The Porphyrin Handbook*, ed. K. M. Kadish, K. M. Smith and R. Guilard, Academic Press, New York, 2000, vol. 1, pp. 239–347.

17 F. A. Walker, in *The Porphyrin Handbook*, ed. K. M. Kadish, K. M. Smith and R. Guilard, Academic Press, New York, 2000, vol. 5, pp. 81–183.

18 Y. Ohgo, S. Neya, T. Ikeue, M. Takahashi, M. Takeda, N. Funasaki and M. Nakamura, *Inorg. Chem.*, 2002, **41**, 4627.

19 Y. Ohgo, T. Ikeue, M. Takahashi, M. Takeda and M. Nakamura, *Eur. J. Inorg. Chem.*, 2004, **4**, 798.

This journal is © The Royal Society of Chemistry 2006

IOP PUBLISHING JOURNAL OF PHYSICS: CONDENSED MATTER

J. Phys.: Condens. Matter **19** (2007) 145215 (6pp) doi:10.1088/0953-8984/19/14/145215

Ageing and memory effects in the weak random anisotropy magnets amorphous NdGdFe and HoGdFe

Toshiaki Saito[1,2], **Ai Emura**[1] **and Koji Hanashima**[1]

[1] Department of Physics, Faculty of Science, Toho University, Funabashi City, Chiba 274-8510, Japan

[2] Research Center for Materials with Integrated Properties, Toho University, Funabashi City, Chiba 274-8510, Japan

Received 29 August 2006
Published 23 March 2007
Online at stacks.iop.org/JPhysCM/19/145215

Abstract

We experimentally examined the ageing phenomena in typical weak random anisotropy magnets (weak RAMs), amorphous NdGdFe and HoGdFe, with a small ratio of the random anisotropy (D) to the ferromagnetic exchange (J) ($D/J \ll 1$). These weak RAMs have very long average relaxation time, two or three orders longer than that of spin glasses (SGs) around the transition temperature, and also have a very large ac excitation field (h_0) dependence of the ac susceptibility. Measuring the imaginary part of the ac susceptibility at frequency of 0.5 Hz and h_0 of 0.3 Oe by using two temperature-change protocols, we observed the memory and rejuvenation effects as reported in SGs, but the effects are weaker in the present weak RAMs, suggesting that the picture of the hierarchical structure of the free energy space is also effective in weak RAMs as in SGs, but it may have smaller barrier heights than those of SGs.

(Some figures in this article are in colour only in the electronic version)

1. Introduction

The magnetic random anisotropy system has frustration due to competition between the uniaxial random anisotropy (D) and the ferromagnetic exchange (J). Weak random anisotropy magnets (weak RAMs) with small D/J ($\ll 1$) have several characteristic properties [1–4] different from both spin glasses (SGs) and 'strong RAMs' [5] with larger D/J (>1). In particular, the dynamical behaviour around the transition temperature (T_c) is remarkable [3]; the magnitude of the imaginary part (Im χ, 90° out of phase component) of the ac susceptibility in weak RAMs such as amorphous (a-)NdGdFe and a-HoGdFe is comparable to that of the real part (Re χ) or even larger than Re χ, which indicates that the average relaxation time is two or three orders larger than that of SGs. Recently [6], we measured the ac field dependence of the ac susceptibility for the weak RAM, a-$(Nd_{0.3}Gd_{0.7})_{19}Fe_{81}$ (T_c is about 290 K), to investigate the origin of the longer relaxation in weak RAMs. The magnitude of ac susceptibility strongly depends on the excitation field, h_0; with increasing h_0, both Re χ and Im χ become several

0953-8984/07/145215+06$30.00 © 2007 IOP Publishing Ltd Printed in the UK

times larger, and the ratio Im χ to Re χ increases for $h_0 < 1$–2 Oe, causing the longer relaxation times in weak RAMs. In addition, temperature width of the peak of Re χ broadens extremely and the peak temperature of Im χ shifts continuously to the lower-temperature side with increasing h_0.

This large h_0 dependence may arise from the free energy structure with small height of barriers due to the small D/J in weak RAMs with weak frustration, compared with that of SGs or strong RAMs; such small barriers with energy height of order of h_0 ($\sim$1 Oe) in weak RAMs may be rather easily surmounted and the system can move to some other local minimum even located far away, which may cause the long relaxation time. Assuming the hierarchical structure of the free energy space also in weak RAM as in SG, we may also explain the broadening of temperature width of Re χ [6].

In this paper, in order to investigate experimentally the structure of free energy in weak RAMs, we examined the ageing phenomena in weak RAMs compared to those of SGs. Although the ageing phenomena (memory and rejuvenation effects, etc) have been extensively studied in SGs [7, 8] and in many glassy systems [9] by using many temperature-change protocols, the ageing phenomena in weak RAMs have not been reported as far as we know.

2. Experimental details

This films of a-$(Nd_{0.9}Gd_{0.1})_{18}Fe_{82}$ and a-$(Ho_{0.6}Gd_{0.4})_{21}Fe_{79}$ (the thicknesses were $\sim$1.5 μm) were prepared by using a magnetron sputtering technique as in our previous works [2–4]. The coherent (not random but uniform) anisotropy of the sample was enough small not to induce the ferromagnetic-like (FWA) phase [1, 4] at static magnetic field $H = 0$ in these samples. Ageing phenomena were observed by measuring the ac susceptibility, in particular, Im χ, by using a SQUID system. The ac excitation field has a frequency (f) of 0.5 Hz and the amplitude (h_0) was 0.3 Oe (small magnitude which hardly affects χ), which was applied parallel to the film plane. The protocols of temperature change for observation of ageing were (1) continuous temperature change with an intermittent stop at T_{ageing} below T_c, and (2) negative and positive temperature cycle at T_{ageing} as described below.

3. Results and discussion

First, we measured the ac susceptibility for a-$(Nd_{0.9}Gd_{0.1})_{18}Fe_{82}$ on cooling the sample from 300 K above T_c ($\sim$221 K) down to 70 K at a constant cooling rate of 1 K min $^{-1}$, and then heating it back continuously at the same rate. The two curves of χ obtained are almost the same. In figure 1, the 'reference curve' of Im χ is shown. We then repeated the measuring, but now stopped at an intermediate temperature T_{ageing} (=210 K) for a certain time, $t_{w0} = 950$ min, only during cooling. During this time t_{w0}, both Re χ and Im χ relax downwards due to ageing. In figure 1, only Im χ is represented because the relative amount of variation of Im χ is much larger than Re χ. In the following we concentrate only on Im χ. After the ageing at 210 K, the cooling procedure resumed. We notice that Im χ merges back with the reference curve at $\sim$200 K (only 10 K below T_{ageing}), indicating that ageing at 210 K does not influence the result at lower temperatures; the chaos effect, as reported in the Heisenberg SG sample $CdCr_{1.7}In_{0.3}S_4$ [7], is also observed in this weak RAM.

When the system is reheated at the same rate, the magnitude of Im χ decreases from the reference curve only around T_{ageing} (from 200 to 220 K), which suggests that the 'memory' of ageing at 210 K has not been erased by the cooling procedure, though the memory is not perfect, as observed in SGs [7], in which even the dip in Im χ at T_{ageing} is exactly recovered.

Second, we examined the negative temperature-cycle protocol for the same sample, a-$(Nd_{0.9}Gd_{0.1})_{18}Fe_{82}$. This protocol consists of the following three stages; (1) the system is

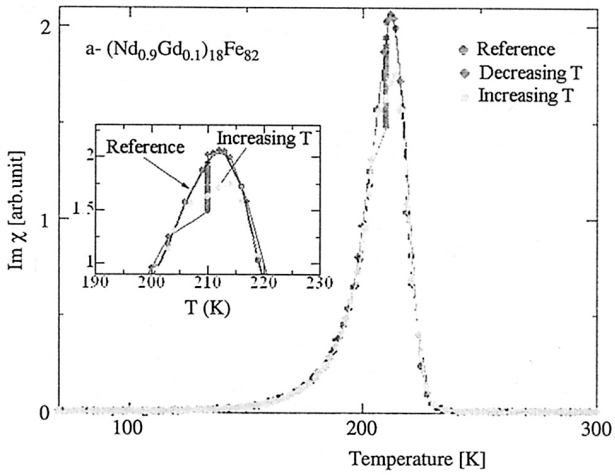

Figure 1. Imaginary part of the ac susceptibility (Im χ) for a weak random anisotropy magnet, a-$(Nd_{0.9}Gd_{0.1})_{18}Fe_{82}$. The measuring frequency is 0.5 Hz, and the ac field is 0.3 Oe. The reference curve was measured continuously at a constant cooling and heating rate of 1 K min^{-1} from 300 K. The measurements of Im χ at the same cooling (decreasing T) and heating (increasing T) rate were performed, except for ageing at 210 K for 950 min (only when decreasing T).

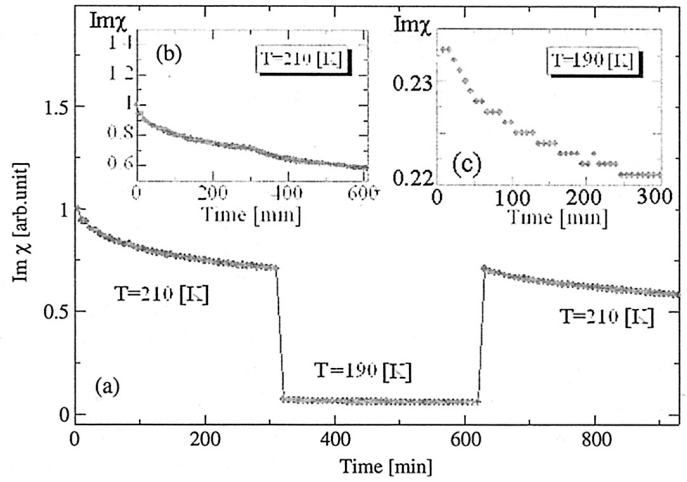

Figure 2. (a) Effect of a negative temperature cycling ($\Delta T/T_{\text{ageing}} \sim 0.1$) on the time dependence of Im χ ($f = 0.5$ Hz, $h_0 = 0.3$ Oe) for a-$(Nd_{0.9}Gd_{0.1})_{18}Fe_{82}$ ($T_c \sim 221$ K). The inset (b) shows a plot of the data points during the first period and the third period at 210 K by removing the second period data at 190 K and by shifting the timescale of the third period. The inset (c) shows the data points during the second period on an extended Im χ scale.

cooled down from 300 K (above T_c) to $T_{\text{ageing}} = 210$ K at 10 K min^{-1}, and is kept at 210 K for a time $t_{w1} = 300$ min, (2) the temperature is temporarily reduced to 190 K ($\Delta T/T_{\text{ageing}} \sim 0.1$) for a time $t_{w2} = 300$ min, (3) then it is set back to 210 K (for 300 min).

Figure 2(a) presents the results on Im χ. (We note that the ac field was zero during the initial cooling process from 300 K to $T_h = 215$ K (5 K above T_{ageing}) and $h_0 = 0.3$ Oe from T_h to T_{ageing}. The following result was the same under the condition of $T_h > T_{\text{ageing}}$.) During

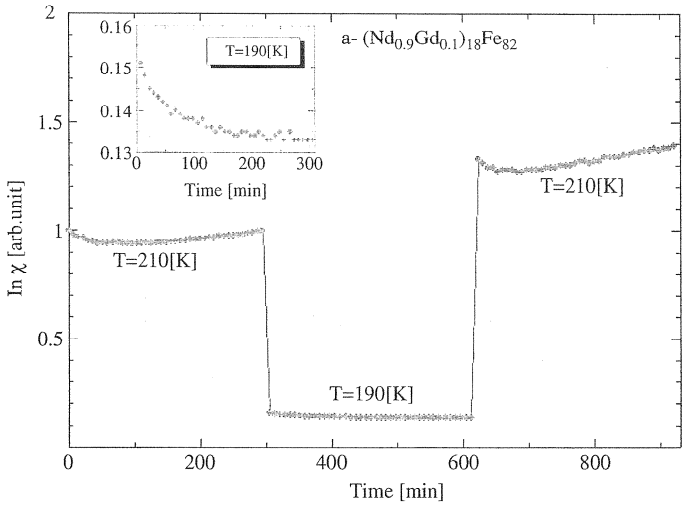

Figure 3. Im χ as a function of time ($f = 0.5$ Hz, $h_0 = 0.3$ Oe) for a-$(Nd_{0.9}Gd_{0.1})_{18}Fe_{82}$ ($T_c \sim 221$ K). It is noted that the excitation field was initially applied at $t = 0$ (h_0 was 0 during the initial cooling process from 300 to 210 K). The inset shows the data points during the second period on an extended Im χ scale.

the first period t_{w1}, the standard relaxation characteristic of ageing is observed. At the first temperature change, a new decay of Im χ occurs at 190 K, as shown in the inset (c) of figure 2 (the second stage), indicating that new ageing starts when the temperature is lowered. At the beginning of the third stage, Im χ returns almost immediately to the standard relaxation with a weak rejuvenation jump. The negative temperature cycle during t_{w2} has not erased the ageing of the first stage during t_{w1}, and then the relaxation is resumed when the temperature is raised back to 210 K (the memory effect) as shown in the inset (b) of figure 2. In the inset, data points at the second stage during t_{w2} at 190 K are removed, and Im χ at the first stage and Im χ at the third stage are directly connected by shifting the timescale of the third period. The best continuation of the data groups of the different two stages seems to require the addition of a small extra time $t_{\rm eff}$ ($\ll t_{w2}$) between the two data groups, even if the small jump of Im χ at the beginning of the third period is excluded (weak memory effect).

These ageing phenomena observed in a weak RAM system imply that the hierarchical structure of the free energy space and a continuous ramification of the metastable states with decreasing temperature are also present in a weak RAM as in SGs. Similar weak rejuvenation by raising the temperature and weak memory effect as shown in figure 2 have been reported for small $\Delta T/T_{\rm ageing}$ ($\sim$0.025) in an SG ($CdCr_{1.7}In_{0.3}S_4$) [8]. Since the ageing process at higher states has also occurred if the decreasing temperature width is small enough (if $\Delta T/T_{\rm ageing}$ is small enough), the system will have effectively aged for $t_{\rm eff}$. In the present weak RAM, the weak rejuvenation and the weak memory effect are observed even for $\Delta T/T_{\rm ageing} \sim 1.0$, which temperature width is not small, at least for an SG ($CdCr_{1.7}In_{0.3}S_4$) [8]. However, the probability of processes across barriers existing at higher temperature may increase if the effective barrier heights are averagely smaller in this weak RAM. This hierarchical picture of free energy space with smaller barrier heights is consistent with our previous experiment [6] in which very strong h_0 dependence of ac susceptibility is observed in weak RAMs as introduced in section 1.

Figure 3 shows the result on Im χ of the same sample in the same condition as in figure 2 except that the ac field was zero during the first cooling process from 300 K ($>T_c$) to 210 K

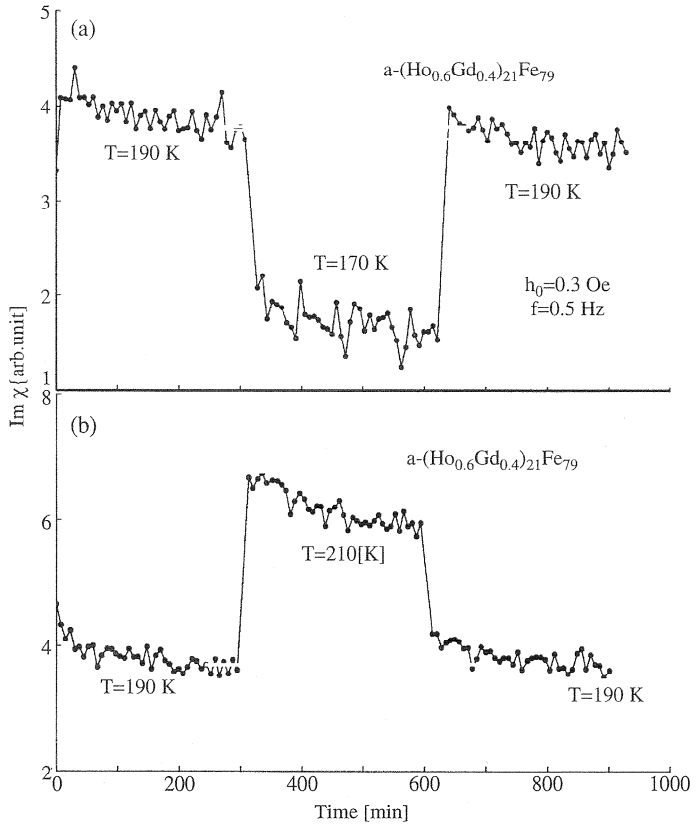

Figure 4. Effect of (a) negative temperature cycling and (b) positive temperature cycling ($\Delta T/T_{\text{ageing}} \sim 0.1$) on the time dependence of Im χ ($f = 0.5$ Hz, $h_0 = 0.3$ Oe) at $T_{\text{ageing}} = 190$ K for a-$(Ho_{0.6}Gd_{0.4})_{21}Fe_{79}$ ($T_c \sim 250$ K).

($T_h = T_{\text{ageing}}$). We found that Im χ does not decrease but continues to increase during the first period t_{w1}, though Im χ initially relaxes at $t \sim 0$. The surprise is that, when the temperature is lowered to 190 K at the beginning of the second stage, the new normal ageing occurs during t_{w2} (see the inset of figure 3) independently of the process in the first stage, and when the temperature is raised back to 210 K at the beginning of the third stage, the increasing of Im χ resumes and Im χ continues to increase during t_{w3} except for the rejuvenation jump at the beginning of the stage. Such distinct temperature independence has not been reported in SGs and other glassy systems as far as we know. The interpretation of this result at 210 K seems to be difficult, but we guess that a kind of 'supercooling' occurs during the initial cooling from 300 K above T_c (=221 K) to 210 K without ac excitation field, and then the system returns to the inherent state at 210 K after the ac field is applied. To clarify this phenomenon, however, further experiments and discussion are needed.

In figure 4 is shown Im χ measured for another weak RAM, a-$(Ho_{0.6}Gd_{0.4})_{21}Fe_{79}$ ($T_c \sim$ 250 K) with slightly smaller D/J than that of a-$(Nd_{0.9}Gd_{0.1})_{18}Fe_{82}$ due to the large amount of Gd ($D \sim 0$). (The signal-to-noise ratio of a-HoGdFe in figure 4 is smaller than that of

a-NdGdFe in figure 2 because the total magnetization of a-HoGdFe is rather small.) Similar ageing effects to a-NdGdFe, which seem to be somewhat weaker due to smaller D/J, are again observed in this weak RAM. For the positive T-cycling protocol (figure 4(b)), the memory of ageing for t_{w1} at the first stage is almost erased when temperature is raised from 190 to 210 K as in an SG [8]. To study the D/J dependence definitely on the ageing effect in weak RAMs, more systematic investigation is needed by controlling D/J, for instance, by observing the ageing effects of a series of a-$(Nd_{1-x}Gd_x)_{18}Fe_{82}$ or a-$(Ho_{1-x}Gd_x)_{21}Fe_{79}$ containing different Gd content (x) (D/J becomes smaller with increasing x).

In conclusion, we observed similar but slightly weaker ageing phenomena in weak RAMs to those of SGs, which suggests that the picture of hierarchical structure of the free energy space is also effective in weak RAM as in SGs, but it may have smaller barrier heights than those of SGs.

References

[1] Chudnovsky E M and Serota R A 1982 *Phys. Rev.* B 26 2697
[2] Saito T, Matsumaru Y, Shinagawa K and Tsushima T 1994 *J. Magn. Magn. Mater.* 130 347
[3] Saito T, Suto A and Takenaka S 2004 *J. Magn. Magn. Mater.* 272–276 1319
[4] Saito T, Mochiduki K, Masago E, Shinagawa K and Tsushima T 1999 *J. Appl. Phys.* 85 4509
[5] Dieny B and Barbara B 1986 *Phys. Rev. Lett.* 57 1169
Sellmyer D J and Nafis S 1986 *Phys. Rev. Lett.* 57 1173
[6] Saito T and Hanashima K 2006 Large ac field dependence of dynamic susceptibility in a weak random anisotropy magnet a-NdGdFe *Proc. ICM2006* at press
[7] Jonason K, Vincent E, Hammann J, Bouchaud J P and Nordblad P 1998 *Phys. Rev. Lett.* 81 3243
[8] Vincent E, Bouchaud J P, Hammann J and Lefloch F 1995 *Phil. Mag.* B **71** 489
[9] For example, Bellon L, Ciliberto S and Laroche C 2000 *Europhys. Lett.* 51 551